Available online at www.sciencedirect.com
SCIENCE DIRECT
Geochimica et Cosmochimica Acta 70 (2006) 3121–3138
Geochimica
www.elsevier.com/locate/gca

Redox equilibria of iron and silicate melt structure: Implications for olivine/melt element partitioning

Bjorn O. Mysen *

Geophysical Laboratory, Carnegie Institution of Washington, 5251 Broad Branch Rd., NW, Washington, DC 20015, USA

Received 13 October 2005; accepted in revised form 29 March 2006

Abstract

Olivine/melt partitioning of ΣFe, Fe^{2+}, Mg^{2+}, Ca^{2+}, Mn^{2+}, Co^{2+}, and Ni^{2+} has been determined in the systems CaO–MgO–FeO–Fe_2O_3–SiO_2 (FD) and CaO–MgO–FeO–Fe_2O_3–Al_2O_3–SiO_2 (FDA3) as a function of oxygen fugacity (f_{O_2}) at 0.1 MPa pressure. Total iron oxide content of the starting materials was ~20 wt%. The f_{O_2} was to used to control the $Fe^{3+}/\Sigma Fe$ (ΣFe: total iron) of the melts. The $Fe^{3+}/\Sigma Fe$ and structural roles of Fe^{2+} and Fe^{3+} were determined with ^{57}Fe resonant absorption Mössbauer spectroscopy. Changes in melt polymerization, NBO/T, as a function of f_{O_2} was estimated from the Mössbauer data and existing melt structure information. It varies by ~100% in melts coexisting with olivine in the FDA3 system and by about 300% in the FD system in the $Fe^{3+}/\Sigma Fe$ range of the experiments (0.805–0.092). The partition coefficients ($D_i^{ol-melt}$ = wt% in olivine/wt% in melt) are systematic functions of f_{O_2} and, therefore, NBO/T of the melt. There is a $D_i^{ol-melt}$-minimum in the FDA3 system at NBO/T-values corresponding to intermediate $Fe^{3+}/\Sigma Fe$ (0.34–0.44). In the Al-free system, FD, where the NBO/T values of melts range between ~1 and ~2.9, the partition coefficients are positively correlated with NBO/T (decreasing $Fe^{3+}/\Sigma Fe$). These relationships are explained by consideration of solution behavior in the melts governed by Q^n-unit distribution and structural changes of the divalent cations in the melts (coordination number, complexing with Fe^{3+}, and distortion of the polyhedra).

1. Introduction

Iron oxide is a major component in natural magmatic liquids (typically the third-most abundant after SiO_2 and Al_2O_3; see http://EarthChem.org). It occurs in two oxidation states, Fe^{3+} and Fe^{2+}, with the redox ratio, Fe^{3+}/Fe^{2+}, on average increasing as magmatic liquids become more felsic (Mysen, 1988, Fig. 8.19, for summary of redox ratios of magmatic liquids).

Equilibrium between ferric and ferrous iron in a silicate melts involves oxygen. Thus, the redox ratio of iron affects silicate melt structure (e.g., Mysen et al., 1984, 1985a; Dingwell and Virgo, 1987). For example, by assuming similar structural roles of Fe^{3+} and Fe^{2+}, decreasing Fe^{3+}/Fe^{2+} causes silicate melt polymerization. With different structural roles of ferric and ferrous iron, the situation becomes more complex (e.g., Dingwell and Virgo, 1987). As a result, any silicate melt property that depends on polymerization also depends on the redox ratio of iron.

Activity–composition relations of major, minor, and trace elements in silicate melts are examples of properties that depend on melt structure (Kushiro, 1975; Ryerson, 1985; Doyle and Naldrett, 1987; Holzheid et al., 1997; O'Neill and Eggins, 2002; Gaillard et al., 2003). Mineral/melt element partition coefficients do, therefore, also depend on melt structure. Factors that can affect the partition coefficients include the ionization potential of network-modifying major element components (Libourel, 1999; Mysen and Dubinsky, 2004; Toplis, 2004), and melt polymerization, NBO/T (Watson, 1977; Mysen and Virgo, 1980; Kohn and Schofield, 1994; Jaeger and Drake, 2000; Toplis and Corgne, 2002; Mysen and Dubinsky, 2004).

* Fax: +1 202 478 8901.
E-mail address: b.mysen@gl.ciw.edu.

0016-7037/$ - see front matter © 2006 Elsevier Inc. All rights reserved.
doi:10.1016/j.gca.2006.03.014

It is possible, therefore, that the redox relations of iron affect mineral/melt partition coefficients. This is so not only because redox equilibria involve oxygen, but also because the structural roles of Fe^{2+} and Fe^{3+} in silicate melts often differ, and also can vary with bulk composition and Fe^{3+}/Fe^{2+} (e.g., Virgo and Mysen, 1985; Dyar et al., 1987; Wang et al., 1993; Burkhard, 2000; Jackson et al., 2005). In minerals, both Fe^{3+} and Fe^{2+} usually are in 6-fold coordination with oxygen. In silicate melts and glasses, 4-, 5-, and 6-fold coordination of Fe^{2+} have been suggested with the coordination number possibly depending on melt composition (Calas and Petiau, 1983; Virgo and Mysen, 1985; Waychunas et al., 1988; Wang et al., 1993; Burkhard, 2000; Rossano et al., 2000; Jackson et al., 2005). For Fe^{3+}, coordination numbers vary between 4 and 6, as for Fe^{2+}. However, available data indicate that 4-fold coordinated Fe^{3+} is most common (Mysen et al., 1980, 1985a; Virgo and Mysen, 1985; Alberto et al., 1996; Holland et al., 1999; Burkhard, 2000; Wilke et al., 2002; Jayasuriya et al., 2004).

Oxygen fugacity, which governs redox equilibria, should, therefore, also affect element partitioning even for cations whose oxidation state does not vary with f_{O_2}. Existing experimental data are, however, somewhat conflicting (Fig. 1). For example, Snyder and Carmichael (1992) show a positive $D_{\Sigma Fe}^{ol\text{-}melt}$ (wt% oxide ratio, olivine/melt) versus

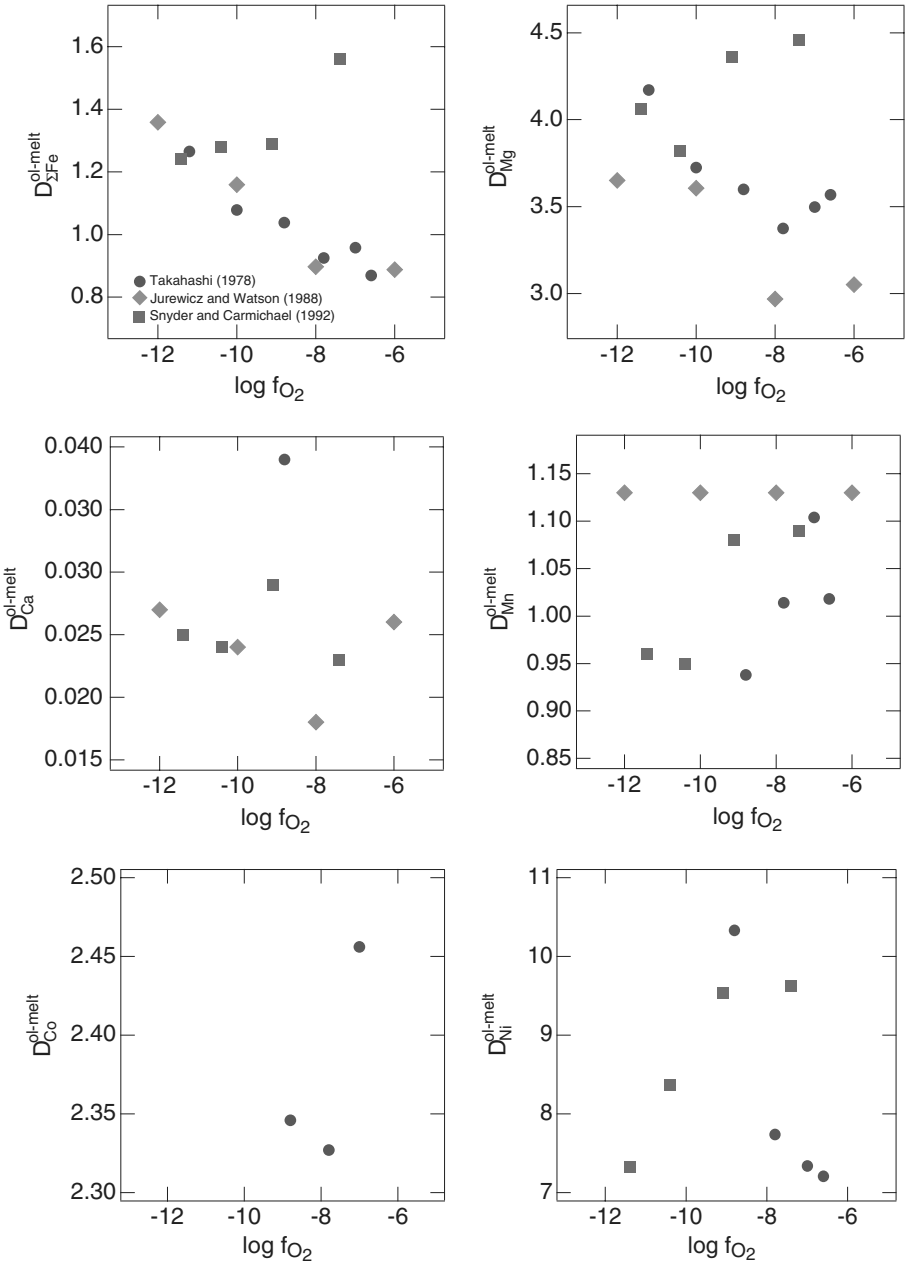

Fig. 1. Literature data on olivine/melt partition coefficients (wt% oxide in olivine/wt% oxide in melt) for total iron (ΣFe), Mg, Ca, Mn, Co, and Ni as a function of oxygen fugacity (f_{O_2}). Data from: Takahashi (1978), Jurewicz and Watson (1988), and Snyder and Carmichael (1992).

f_{O_2} correlation, whereas Takahashi (1978) and Jurewicz and Watson (1988) reported the opposite relationship (Fig. 1). The $D_{Mg}^{ol\text{-}melt}$ exhibits a similar relationship to f_{O_2} (Fig. 1). For other elements, such as Ca, Mn, Co, and Ni, the data show considerable scatter. These differences and data scatter may at least in part result from the fact that melt and mineral compositions in the published studies differ significantly from each other with bulk compositions ranging from K- and Mg-rich silicate (Takahashi, 1978; Jurewicz and Watson, 1988) to basic natural melts (Snyder and Carmichael, 1992).

It is possible, indeed likely, that the features in Fig. 1 can be related to variations in major element melt composition as a function of f_{O_2}, and, therefore, redox ratio of iron. There is, however, little quantitative information on how redox relations of iron in silicate melts influence the distribution of major, minor, and trace elements between minerals and melts. This is the topic of the present report.

The objective was to address how the olivine/melt partition coefficients of Ca and 1.-row transition elements may respond to changes of redox relations of iron and possible consequent changes of the melt structure. Of these metals, Ni^{2+} and Mn^{2+} most likely occupy distorted octahedral, whereas Co^{2+} may have a smaller coordination number (Keppler, 1992; Keppler and Bagdassarov, 1999). The Ca coordination number likely is 6 or greater, and depends on whether Ca serves to charge-balance Al^{3+} in tetrahedral coordination or is a network-modifying cation (Binsted et al., 1985). These features may themselves depend on melt structure and require evaluation.

2. Experimental methods

Starting materials were two compositions, FD and FDA3, in the systems CaO–MgO–FeO–Fe_2O_3–SiO_2 and CaO–MgO–FeO–Fe_2O_3–Al_2O_3–SiO_2 to which were added MnO, CoO, and NiO. Most experiments were conducted with 1 wt% of the latter three oxides added. Experiments were also done with 0.5, 1.5, and 2.0 wt% of these oxides in order to address whether or not there were deviations from Henry's law. The nominal compositions of these materials are listed in Table 1.

The starting materials were made in batches of about 1 gram from spectroscopically pure oxide mixtures (SiO_2, Al_2O_3, Fe_2O_3, MgO, MnO, NiO, and Co_3O_4) +$CaCO_3$ mixed by grinding under alcohol in an agate mortar for about 1 h. $CaCO_3$ is converted to CaO and CO_2 during heating of these mixtures (breakdown temperature if $CaCO_3$ is near 1200 °C at ambient pressure) to experimental temperature. CO_2 is released to the ambient atmosphere and does not affect the experiments. These starting materials were stored at 110 °C when not in use.

Table 1
Composition of starting materials

	FDA3-0.5	FDA3	FDA3-1.5	FDA3-2.0	FD
SiO_2	40.63	40.02	39.56	38.77	39.99
Al_2O_3	10.15	10.00	9.88	9.69	0.00
FeO	20.32	20.00	19.78	19.38	20.01
MnO	0.50	0.99	1.48	2.01	1.00
MgO	18.28	18.01	17.52	17.45	28.01
CaO	9.13	9.00	8.75	8.72	9.00
CoO	0.49	0.98	1.51	1.99	1.00
NiO	0.50	1.00	1.51	2.00	1.00

Experiments were conducted at ambient (0.1 MPa) pressure in vertical $MoSi_2$-heated furnaces with CO–CO_2 gas mixtures to control the oxygen fugacity. The f_{O_2} was monitored with an Y-stabilized ZrO_2 electrochemical cell (Tretyakov and Muan, 1969; Sato, 1972). The f_{O_2} is precise to better than 1%. The accuracy, measured against the Ni–NiO and Fe–FeO reactions, is better than 0.1 log unit. The temperature was measured with a Pt–$Pt_{90}Rh_{10}$ thermocouple located within 1 cm of the sample. The hot zone (±1 °C) is ~3 cm long in these furnaces. Temperature precision is ±1 °C. Its accuracy, measured against the melting point of Au, is ±3 °C.

The starting materials were suspended on 0.1 mm, iron-saturated Pt-wires to minimize loss of transition metals to the sample containers (Presnall and Brenner, 1974). Fe-saturation was carried out with Pt-wire suspended in melts of the two starting compositions, held at 1450 °C for 24 h. The sample/wire wt ratio was approximately 100/1. The experiments were terminated by quenching in liquid water with a quenching rate of approximately 500 °C/s.

The experimental charges, consisting of 50–100 μm euhedral olivine crystals, glass, and sometimes magnesioferrite or Al–spinel,[1] were analyzes with a JEOL 8900 electron microprobe operating at 15 kV with 10 nA beam current. Counting time on both peak and background was 30 s. For these analytical conditions, the peak-to-background even for the lowest Ni contents (Ni in melt equilibrated at $f_{O_2} = 10^{-8}$) is about 5/1. By defining detection limit as that of a peak-to-background of 2/1, this converts to about 100 ppm NiO (0.01 wt% NiO) For olivine crystals, the analyses were typically carried out by randomly selecting at least 20 analytical points. Glass was analyzed by rastering the electron beam over 10 × 10 μm squares typically with about 10 squares per experimental charge. The average of these analyses together with the standard error of the average was used to represent the chemical compositions of the coexisting olivine and melts (Table 2).

The CaO content of olivine from electron microprobe analysis near olivine/glass interfaces may be affected by the CaO in glass adjacent to olivine (e.g., Jurewicz and Watson, 1988) because of the low CaO concentration in olivine (<1 wt% CaO; Table 2) compared with that of the glass (wt% $CaO^{olivine}$/wt% CaO^{glass} typically is less than 0.05—see also Table 2). The extent to which this could be a problem was assessed by analytical traverses across olivine grains as reported in more detail by Mysen and Dubinsky (2004). No analytical points of olivine less than

[1] Magnesioferrite coexists with olivine and melt in experimental charges from the FD composition at f_{O_2} near that of air. Al–spinel coexists with olivine and melt in experimental charges from FDA3 at $f_{O_2} \leqslant 10^{-4}$.

Table 2
Experimental results

Comp	FDA3		FDA3		FDA3		FDA3	
Temperature (°C)	1300		1300		1300		1300	
log f_{O_2}	−0.68		−0.68		−0.68		−0.68	
Time (min)	400		945		1380		3570	
	Glass	Olivine	Glass	Olivine	Glass	Olivine	Glass	Olivine
SiO_2	46.33(61)[b]	41.79(85)	46.49(42)	41.24(20)	46.54(37)	41.16(22)	45.81(21)	41.25(27)
Al_2O_3	11.89(15)	0.19(19)	11.71(14)	0.16(17)	11.70(7)	0.089(9)	11.90(10)	0.073(8)
FeO	12.97(45)	3.20(24)	13.25(11)	3.21(10)	13.11(13)	3.16(11)	12.78(12)	2.95(6)
MgO	15.12(19)	52.93(184)	15.02(19)	52.66(57)	14.93(8)	52.53(10)	14.60(7)	51.68(146)
CaO	11.078(25)	0.39(14)	10.88(19)	0.29(3)	11.19(12)	0.24(2)	11.36(8)	0.32(7)
MnO	0.84(4)	0.66(6)	0.94(3)	0.68(2)	0.94(2)	0.68(1)	0.95(2)	0.67(2)
CoO	0.63(3)	1.26(13)	0.65(3)	1.34(4)	0.62(3)	1.26(5)	0.60(3)	1.30(4)
NiO	0.33(3)	2.16(15)	0.30(2)	2.35(3)	0.32(2)	2.29(3)	0.31(2)	2.28(4)
Total	99.17	102.57	99.17	101.94	99.34	101.41	98.29	100.51
Fo		96.72		96.69		96.73		96.9
$Fe^{3+}/\Sigma Fe$	0.80[a]		0.80[a]		0.805		0.80[a]	
NBO/T	0.65		0.64		0.64		0.64	
$D_{Fe^{2+}}^{ol\text{-}melt}$	1.17(1)[c]		1.156(1)		1.187(2)		1.10(10)	
$D_{Mg}^{ol\text{-}melt}$	3.32(12)		3.35(6)		3.38(2)		3.39(9)	
$D_{Ca}^{ol\text{-}melt}$	0.03(1)		0.0256(2)		0.021(1)		0.0267(6)	
$D_{Mn}^{ol\text{-}melt}$	0.75(7)		0.68(3)		0.69(2)		0.68(3)	
$D_{Co}^{ol\text{-}melt}$	1.90(21)		1.97(10)		1.95(12)		2.09(12)	
$D_{Ni}^{ol\text{-}melt}$	6.32(74)		7.38(47)		6.83(41)		7.08(52)	
Comp	FDA3-0.5		FDA3-1.5		FDA3-2		FDA3	
Temperature (°C)	1300		1300		1300		1300	
log f_{O_2}	−0.68		−0.68		−0.68		−3	
Time (min)	1500		1625		1340		1370	
	Glass	Olivine	Glass	Olivine	Glass	Olivine	Glass	Olivine
SiO_2	45.56(15)	40.58(84)	46.51(4)	40.36(18)	45.07(19)	39.95(40)	43.50(35)	39.78(43)
Al_2O_3	11.55(3)	0.09(1)	11.69(4)	0.17(2)	11.52(5)	0.18(18)	12.01(9)	0.12(30
FeO	14.15(9)	3.27(9)	12.06(7)	3.90(11)	12.13(13)	3.12(22)	15.94(14)	6.86(11)
MgO	15.82(7)	53.55(34)	14.00(11)	48.71(166)	14.26(8)	48.80(60)	14.14(9)	48.16(24)
CaO	10.90(7)	0.24(2)	11.48(8)	0.60(7)	11.39(7)	0.36(19)	10.84(7)	0.36(4)
MnO	0.5292)	0.34(2)	1.45(2)	1.06(2)	2.04(3)	1.46(2)	0.99(1)	0.73(2)
CoO	0.34(2)	0.70(2)	0.90(4)	1.97(3)	1.30(3)	2.62(4)	0.75(20)	1.43(20)
NiO	0.18(2)	1.27(2)	0.45(3)	3.18(11)	0.68(2)	4.28(7)	0.41(2)	2.67(5)
Total	99.03	100.05	98.52	99.95	98.40	100.77	98.58	100.12
Fo		96.68		95.7		96.54		92.59
$Fe^{3+}/\Sigma Fe$	0.80[a]		0.80[a]		0.80[a]		0.575	
NBO/T	0.65		0.66		0.72		0.81	
$D_{Fe^{2+}}^{ol\text{-}melt}$	1.112(1)		1.582(2)		1.243(3)		0.978(3)	
$D_{Mg}^{ol\text{-}melt}$	3.25(3)		3.41(12)		3.31(4)		3.29(3)	
$D_{Ca}^{ol\text{-}melt}$	0.021(2)		0.052(6)		0.03(2)		0.032(4)	
$D_{Mn}^{ol\text{-}melt}$	0.63(4)		0.71(2)		0.69(1)		0.72(2)	
$D_{Co}^{ol\text{-}melt}$	1.98(11)		2.15(9)		1.95(5)		1.84(5)	
$D_{Ni}^{ol\text{-}melt}$	6.77(64)		7.00(48)		6.09(19)		6.33(28)	
Comp	FDA3		FDA3		FDA3		FDA3	
Temperature (°C)	1300		1300		1300		1300	
log f_{O_2}	−4		−5		−6		−7	
Time (min)	1380		4240		1410		1400	
	Glass	Olivine	Glass	Olivine	Glass	Olivine	Glass	Olivine
SiO_2	40.98(25)	39.39(31)	41.14(11)	39.29(35)	41.02(10)	38.86(27)	40.51(50)	38.28(47)
Al_2O_3	12.32(8)	0.13(3)	12.54(6)	0.13(2)	13.31(19)	0.17(6)	13.50(10)	0.14(8)
FeO	19.54(7)	9.87(15)	19.39(32)	11.37(14)	19.69(12)	14.96(8)	18.91(10)	16.89(11)
MgO	13.34(8)	43.78(18)	12.85(16)	44.46(37)	12.19(10)	42.17(24)	11.93(24)	41.26(19)
CaO	12.06(4)	0.36(2)	10.59(11)	0.36(3)	10.96(12)	0.43(2)	11.93(6)	0.50(3)
MnO	0.99(2)	0.71(1)	0.97(20	0.76(2)	0.97(2)	0.81(1)	1.02(3)	0.87(2)
CoO	0.77(4)	1.47(4)	0.76(3)	1.54(4)	0.77(3)	1.49(3)	0.65(2)	1.33(4)
NiO	0.46(2)	2.60(3)	0.49(2)	2.85(9)	0.38(2)	2.36(4)	0.23(2)	1.39(3)
Total	100.46	98.31	98.72	100.74	99.30	101.24	98.67	100.67

Table 2 (*continued*)

	Glass	Olivine	Glass	Olivine	Glass	Olivine	Glass	Olivine
Fo		88.72		87.45		81.32		81.32
$Fe^{3+}/\Sigma Fe$	0.447		0.436[a]		0.232		0.172[a]	
NBO/T	1.044		0.902		1.282		1.417	
$D_{Fe^{2+}}^{ol\text{-}melt}$	0.915(4)		0.863(8)		0.965(5)		1.058(6)	
$D_{Mg}^{ol\text{-}melt}$	3.27(2)		3.33(5)		3.37(3)		3.39(7)	
$D_{Ca}^{ol\text{-}melt}$	0.030(2)		0.032(2)		0.039(2)		0.041(3)	
$D_{Mn}^{ol\text{-}melt}$	0.72(2)		0.75(3)		0.81(2)		0.84(3)	
$D_{Co}^{ol\text{-}melt}$	1.91(10)		1.95(9)		1.87(9)		2.01(9)	
$D_{Ni}^{ol\text{-}melt}$	5.67(25)		5.59(31)		6.01(28)		5.91(61)	
Comp	FDA3		FD		FD		FD	
Temperature (°C)	1300		1375		1375		1375	
log f_{O_2}	−8		−0.68		−0.68		−0.68	
Time (min)	1425		440		1320		5320	
	Glass	Olivine	Glass	Olivine	Glass	Olivine	Glass	Olivine
SiO_2	42.52(17)	38.40(21)	41.58(28)	40.25(62)	43.96(32)	40.53(52)	43.26(82)	40.62(23)
Al_2O_3	14.05(8)	0.079(6)	0.041(5)	0.001(2)	0.11(13)	0.44(55)	0.044(7)	0.001(2)
FeO	16.98(17)	16.73(5)	23.55(47)	4.52(112)	22.15(35)	3.78(12)	22.26(43)	3.69(7)
MgO	12.25(6)	42.19(20)	18.47(64)	50.20[a](86)	17.85(28)	49.67(88)	16.91(62)	50.61(32)
CaO	12.17(5)	0.47(1)	12.73(26)	0.51(4)	12.85(17)	0.57(6)	13.15(16)	0.45(1)
MnO	1.03(1)	0.92(2)	1.07(2)	0.65(3)	1.04(3)	0.65(2)	1.03(2)	0.64(2)
CoO	0.48(2)	1.05(4)	0.77(2)	1.18(3)	0.73(4)	1.15(3)	0.73(3)	1.14(4)
NiO	0.08(2)	0.54(2)	0.49(4)	1.69(4)	0.46(3)	1.69(3)	0.51(3)	1.76(4)
Total	99.55	100.39	98.700	99.00	99.15	98.47	97.72	98.90
Fo		81.79		95.19		95.91		96.08
$Fe^{3+}/\Sigma Fe$	0.118		0.827[a]		0.792		0.827[a]	
NBO/T	1.304		1.039		1.028		0.981	
$D_{Fe^{2+}}^{ol\text{-}melt+}$	1.120(9)		0.998(7)		0.719(1)		0.859(1)	
$D_{Mg}^{ol\text{-}melt}$	3.45(2)		2.44(9)		2.65(5)		2.68(10)	
$D_{Ca}^{ol\text{-}melt}$	0.0389(1)		0.036(3)		0.039(4)		0.030(7)	
$D_{Mn}^{ol\text{-}melt}$	0.90(2)		0.55(2)		0.55(2)		0.56(2)	
$D_{Co}^{ol\text{-}melt}$	2.20(12)		1.38(5)		1.36(8)		1.40(7)	
$D_{Ni}^{ol\text{-}melt}$	6.64(156)		3.09(25)		3.27(21)		3.12(18)	
Comp	FD		FD		FD		FD	
Temperature (°C)	1375		1375		1375		1375	
log f_{O_2}	−2.65		−4		−6.5		−8	
Time (min)	1395		1430		1625		1350	
	Glass	Olivine	Glass	Olivine	Glass	Olivine	Glass	Olivine
SiO_2	39.73(33)	39.02(57)	37.72(12)	39.33(14)	41.04(44)	36.86(39)	44.06(27)	37.90(22)
Al_2O_3	0.06(1)	0.001(2)	0.013(8)	0.01(2)	0.019(3)	0.005(7)	0.02(2)	0.01(4)
FeO	26.08(53)	8.98(10)	27.19(15)	11.46(9)	23.00(20)	15.85(11)	20.05(14)	16.05(16)
MgO	16.32(125)	47.23(22)	13.72(38)	44.66(31)	13.32(74)	41.77(16)	15.09(48)	42.54(20)
CaO	13.15(90)	0.63(3)	17.50(23)	1.07(3)	18.36(50)	1.30(1)	17.24(26)	1.13(2)
MnO	1.14(5)	0.73(2)	1.16(2)	0.88(2)	1.11(2)	0.91(3)	1.14(3)	0.91(3)
CoO	0.85(5)	1.12(3)	0.78(2)	1.11(3)	0.71(3)	1.06(3)	0.49(2)	0.82(2)
NiO	0.43(4)	1.67(3)	0.40(3)	1.53(3)	0.24(3)	1.07(2)	0.07(2)	0.41(3)
Total	97.77	99.38	98.479	100.05	97.81	98.82	98.17	99.79
Fo		90.36		87.41		82.44		82.53
$Fe^{3+}/\Sigma Fe$	0.638[a]		0.587		0.172		0.092	
NBO/T	1.39		1.756		2.9		2.683	
$D_{Fe^{2+}}^{ol\text{-}melt}$	0.847(3)		0.896(1)		0.775(6)		0.835(8)	
$D_{Mg}^{ol\text{-}melt}$	2.57(20)		2.86(8)		2.92(16)		2.67(9)	
$D_{Ca}^{ol\text{-}melt}$	0.043(4)		0.054(2)		0.066(2)		0.062(1)	
$D_{Mn}^{ol\text{-}melt}$	0.57(3)		0.66(2)		0.76(3)		0.75(3)	
$D_{Co}^{ol\text{-}melt}$	1.17(7)		1.25(5)		1.38(7)		1.59(9)	
$D_{Ni}^{ol\text{-}melt}$	3.43(29)		3.33(28)		4.11(50)		5.52(140)	

[a] $Fe^{3+}/\Sigma Fe$ calculated as described in text.

[b] Numbers in parentheses represent standard error of average.

[c] Calculated from standard error of average of glass and olivine compositions.

~20 μm from an olivine/glass interface was used to avoid interference from Ca in neighboring glass.

The lowest-f_{O_2} experiments were conducted at f_{O_2}-values 2–3 orders of magnitude below the nickel–nickel oxide equilibrium. There is, nevertheless, no evidence of metallic Ni or Ni-bearing alloys in the experimental charges. This is likely because (i) redox equilibria in crystalline oxides cannot be employed to characterize the equilibria in structurally quite different silicate melts, and (ii) the nickel contents of the run products are on the order of 1%, and, thus greatly diluted compared with the Ni–O system. This conclusion does not rule out, however, the some metal, in particular Ni may dissolve in the Pt-wires used for sample suspension in the furnace. The short-duration Ni experiments show somewhat greater errors than those of the other compositions. This is likely because some portion of the nickel in the starting material dissolves in the Pt hanging wire during the first several hundred minute experimental durations.

Time studies were employed to assess the time needed to reach equilibrium (Fig. 2). Experimental run durations were kept near 24 h (Table 2). Longer experimental durations do not affect the partition coefficients.

The structural behavior of Fe^{2+} and Fe^{3+} in quenched melts (glass) was examined with ^{57}Fe resonant absorption

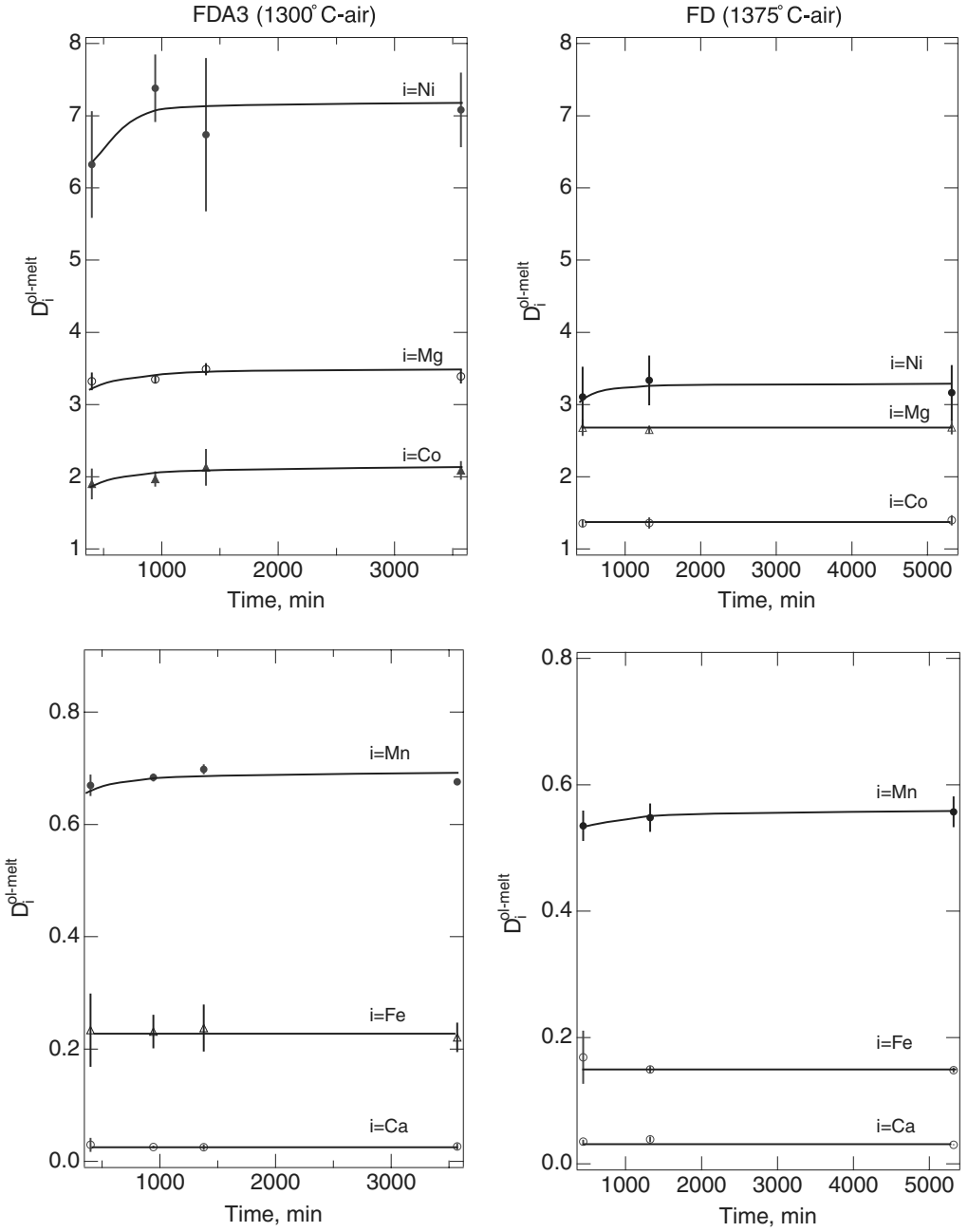

Fig. 2. Nickel, Mg, and Mn olivine/melt partition coefficients as a function of experimental duration at 1300 °C (FDA3) and 1375 °C (FD) in at $f_{O_2} = 10^{-0.68}$ (air).

Mössbauer spectroscopy. For this purpose, glass compositions from several different run products at different f_{O_2} were remade and transformed to melt at the original temperature before being quenched to a glass. These samples were prepared for Mössbauer spectroscopy by crushing the glass to a fine powder and mixed with transoptic powder. This mixture was converted to 12.7-mm diameter pellets at 350 bar and 120 °C. The resulting pellets, containing about 50 mg sample and about 100 mg transoptic powder, were about 1 mm thick.

The Mössbauer experiments were conducted with a ~40 mCi ^{57}Co flat source with the drives (Austin Science) operating in constant acceleration mode between −4 and 4 mm/s. The isomer shifts of Fe^{3+} and Fe^{2+}, $\delta_{Fe^{3+}}$ and $\delta_{Fe^{2+}}$, are reported relative to Fe metal.

The Mössbauer spectra were deconvoluted by using the site-distribution method of Alberto et al. (1996). With this method, the site distribution function, $S_i(v)$, is related to the probability distribution function, $P(\delta_i, \Delta_i, \sigma_{\delta_i}, \sigma_{\Delta_i}, \theta_i)$, of the absorption doublet, $D(v, \delta_i, \Delta_i, \omega, I_i)$ as (Alberto et al., 1996):

$$S_i(v) = \int\int P(\delta_i, \Delta_i, \sigma_{\delta_i}, \sigma_{\Delta i}, \theta_i) \cdot D(v, \delta_i, \Delta_i, \omega, I_i) \mathrm{d}\delta_i \mathrm{d}\Delta_i, \quad (1)$$

Here, v is velocity, δ_i and Δ_i are isomer shift and quadrupole splitting, with respective standard deviations, $\sigma_{\delta i}$ and σ_{Δ_i}. The intensity is I_i. The θ_i is a correlation parameter between isomer shift and quadrupole splitting. These are independent variables in this deconvolution procedure. The fitting was conducted with the width of the elementary absorption peaks, ω, constant and equal to that of elemental Fe.

3. Results

Before examination of possible effects of melt composition and structure on element partitioning, we need to address whether the activity–composition relations in the olivine vary significantly over the concentration intervals employed here. As seen in Fig. 3, straight-line fits passing near the origin of the concentrations of MnO, CoO, and NiO in olivine and coexisting melt suggest that the solubility behavior of these elements in neither the melt nor the olivine varies over these concentration ranges. This observation is consistent with manganese partitioning between forsterite and melt in Fe-free systems, which was reported to behave similarly in the same concentration range (Watson, 1977; Jurewicz and Watson, 1988). These observations are also consistent with thermodynamic data for Ca-, and Mn-bearing forsterite (Schwerdtfeger and Muan, 1966; Warner and Luth, 1974). For olivine in the Ni_2SiO_4–Mg_2SiO_4 and Co_2SiO_4–Mg_2SiO_4 systems, a small positive deviation from ideal mixing has been reported (Seifert and O'Neill, 1987). However, crystal chemical data from Ni_2SiO_4–Mg_2SiO_4 olivine solid solutions interpolated to the low-concentration range relevant to the present study show that the unit cell volume is a linear function of Ni/(Ni + Mg) (Boström, 1987; Ottonello et al., 1989). Thus, one would not expect the activity–composition relations in this olivine to vary in this composition range. It has, nevertheless, been suggested that the Fo content of olivine may affect partition coefficients of Ca, for example (Toplis and Carroll, 1995). However, olivine composition was not an independent variable either in the experiments of Toplis and Carroll (1995) or in the present experiments. The Fo content depends on the oxygen fugacity, which also affects melt composition (Table 2). Such data by themselves cannot, therefore, to establish whether olivine compositional changes affect the olivine/melt partition coefficients. In light of the discussion above of existing composition–activity relations in olivine as well the composition-independent partition coefficients (Fig. 3), it is not likely that the partitioning behavior is controlled by the olivine compositions.

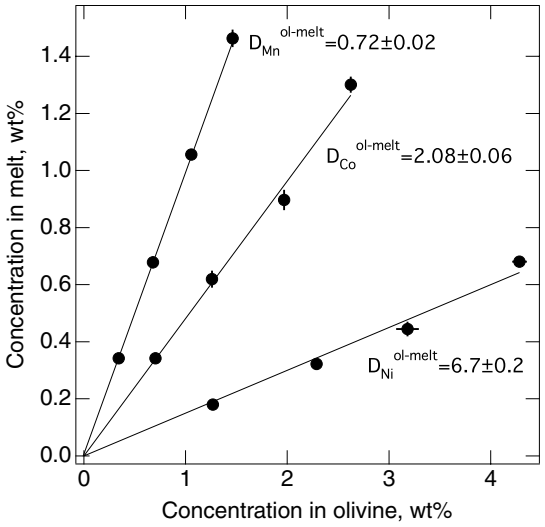

Fig. 3. Nickel, Mg, and Mn olivine/melt partition coefficients for composition FDA3 as a function of Ni, Mg, and Mn concentration in olivine and melt. Experiments were conducted with the f_{O_2} of air and at 1300 °C.

3.1. Olivine/melt partitioning and oxygen fugacity

The olivine/melt partition coefficients ($D_i^{ol\text{-}melt}$ = wt% oxide in olivine/wt% oxide in melt) for ΣFe (total iron), Mg, Ca, Mn, Co, and Ni as a function of f_{O_2} are shown in Fig. 4. Analytical data are provided in Table 2.

The $D_{\Sigma Fe}^{ol\text{-}melt}$ increases systematically with decreasing f_{O_2} in a manner qualitatively similar to that reported by Takahashi (1978) and Jurewicz and Watson (1988) (Fig. 1). This trend most likely is governed by the variable oxidation state of iron in the melts.

The $D_{Mn}^{ol\text{-}melt}$ also increases with decreasing oxygen fugacity although the decrease is less than 50% of that of $D_{\Sigma Fe}^{ol\text{-}melt}$ (Fig. 4). This relationship could possibly be caused by changes in the redox state of Mn. From their experimental data relating the Ca,Mn-exchange

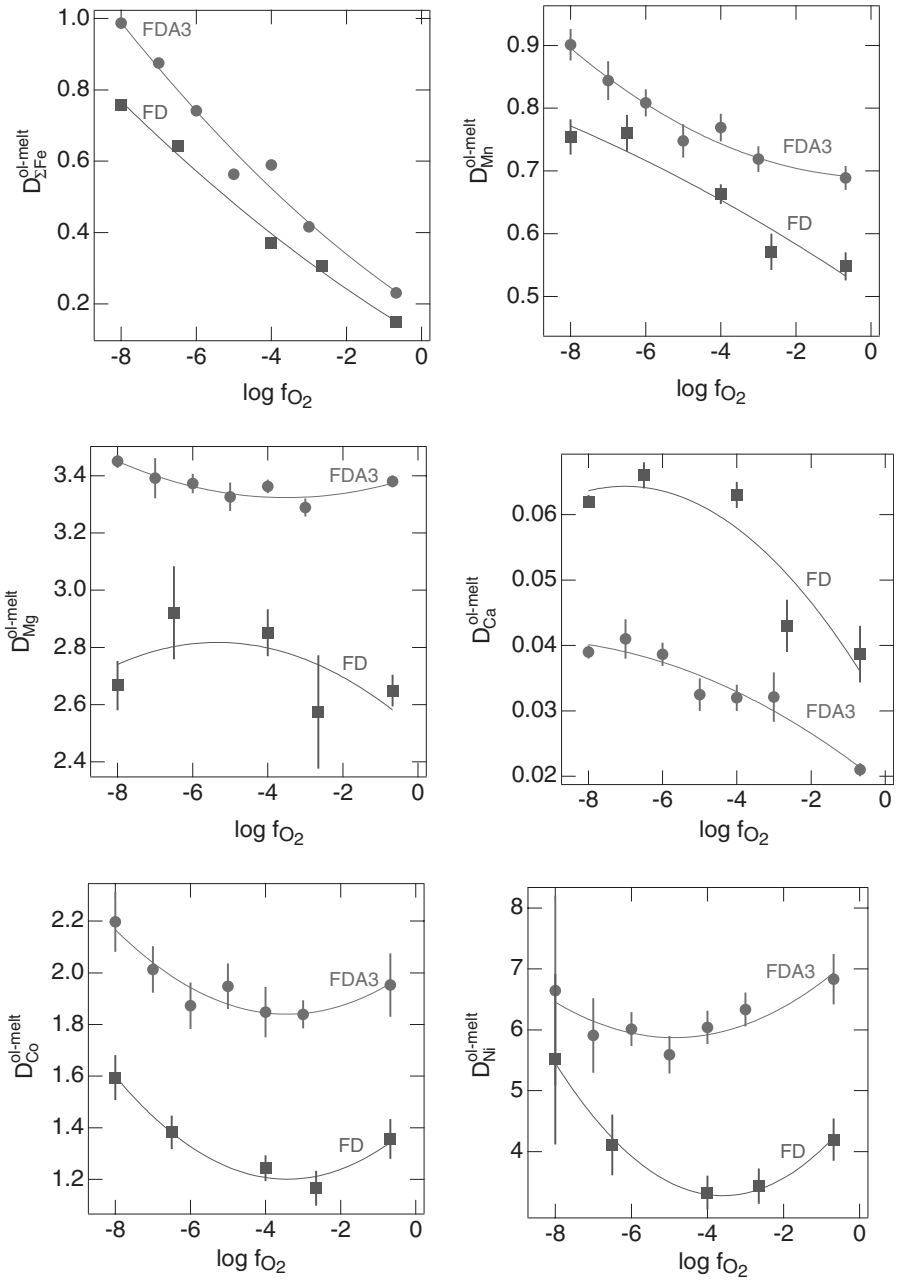

Fig. 4. Olivine/melt partition coefficients, $D_{\Sigma Fe}^{ol\text{-}melt}$, $D_{Mn}^{ol\text{-}melt}$, $D_{Mg}^{ol\text{-}melt}$, $D_{Ca}^{ol\text{-}melt}$, $D_{Co}^{ol\text{-}melt}$, and $D_{Ni}^{ol\text{-}melt}$ as a function of oxygen fugacity, f_{O_2}, for the systems FDA3 (1300 °C) and FD (1375 °C). The lines are 3.-order polynomial fits to the data.

equilibrium between olivine and melt to f_{O_2}, Mysen and Dubinsky (2004) concluded that even at the oxygen fugacity of air at least 75% of the manganese exists as Mn^{2+}. They also noted agreement between their $D_{Mn}^{ol\text{-}melt}$-values with published data obtained both at low f_{O_2} and in air. That agreement would suggest that even if there is a small fraction of Mn as Mn^{3+} in the melts, the assumption that manganese exists as Mn^{2+} does not introduce significant errors. We will, therefore, discuss manganese partitioning behavior as if it exists only as Mn^{2+} in the melts. All Mn in olivine is assumed to be Mn^{2+}. One might suggest, therefore, that changes in melt composition (structure) resulting from changes of f_{O_2} is a more likely explanation for the $D_{Mn}^{ol\text{-}melt}$ trends in Fig. 4. This suggestion is further substantiated by the behavior of $D_{Ca}^{ol\text{-}melt}$, which increases by about 100 % in the f_{O_2}-range between $10^{-0.68}$ and 10^{-8}. Variable oxidation state of calcium cannot be invoked to explain the $D_{Ca}^{ol\text{-}melt}$ behavior.

The olivine/melt partition coefficients for the other divalent cations, Mg^{2+}, Co^{2+}, and Ni^{2+}, also depend on oxygen fugacity (Fig. 4). There are distinct minima or maxima at intermediate f_{O_2}-values. In the FD system, neither maxima nor minima occur. The partition coefficients are also distinctly dependent on the starting compositions (Table 2;

Fig. 4). With the exception of $D_{Ca}^{ol\text{-}melt}$, the olivine/melt partition coefficients are higher for the FDA3 starting compositions than for FD.

3.2. Redox relations of iron

Oxygen fugacity governs the redox ratio of iron. That ratio, in turn, can affect the melt structure. To determine Fe^{3+}/Fe^{2+} and the structural behavior of Fe^{3+} and Fe^{2+} in the melts, Mössbauer spectra were obtained for 8 of the melts coexisting with olivine as a function of f_{O_2} (Fig. 5).

The Mössbauer spectra exhibit two or three major absorption peaks, as is typical for spectra of Fe-bearing glasses (e.g., Mysen et al., 1980, 1984, 1985a,b; Dyar et al., 1987; Wang et al., 1993; Johnson et al., 1999; Rossano et al., 1999; Burkhard, 2000; Wilke et al., 2002; Jayasuriya et al., 2004). The low-velocity peak (between about 0 and −0.5 mm/s) includes the low-velocity components of both Fe^{2+} and Fe^{3+} and shifts to slightly higher velocity with decreasing f_{O_2} (Fig. 5). The high-velocity peak, near 2 mm/s, grows in intensity with decreasing f_{O_2}, whereas the absorption between 0.5 and 1 mm/s becomes less intense as the oxygen fugacity decreases. The high-velocity absorption is due to Fe^{2+}, whereas the absorption at intermediate velocity is due to Fe^{3+}.

The Mössbauer spectra were deconvoluted to obtain the redox ratio of iron and the hyperfine parameters (quadrupole splitting, Δ, and isomer shift, δ) of ferric and ferrous iron. In this deconvolution procedure (Alberto et al., 1996), it is assumed that the spectra can be described in terms of Gaussian distribution of isomer shifts and quadrupole splitting, similar to the approach advocated elsewhere (Lagarec and Rancourt, 1997; Rossano et al., 1999; Wilke et al., 2002; Jayasuriya et al., 2004). The number of site distributions was determined by evaluating the χ^2 from the resulting fit. The spectra were deconvoluted satisfactorily with one distribution for Fe^{3+} and one for Fe^{2+}.

Examples of the total probability function, $P(\delta_i, \Delta_i, \sigma_{\delta_i}, \sigma_{\Delta_i}, \theta_i)$, and the distribution of the absorption doublets, $D(v,\delta_i,\Delta_i,\omega,\ I_i)$, from such fits of an oxidized and reduced glass are shown in Fig. 6. Data from the fits of all the spectra are given in Table 3.

The ferric/ferrous ratio was obtained from the relative areas of the absorption doublets (see Fig. 6C and D). There are, however, small differences in recoil-free fractions of Fe^{3+} and Fe^{2+}, which can affect the Fe^{3+}/Fe^{2+} ratio derived from the spectra (Virgo and Mysen, 1985; Alberto et al., 1996) although Jayasuriya et al. (2004) suggested that the differences were so small that the temperature at which Mössbauer spectra were obtained does not affect the redox ratio derived from the area ratio of the absorption doublets. Mysen and Richet (2005) (their Figs. 10.3 and 10.4) used the data of Mysen et al. (1985b) and Dingwell (1991) to compare Fe^{3+}/Fe^{2+} from Mössbauer spectra (recorded at 298 K) and from wet chemical methods. They did not see any bias in the redox ratios thus determined. Suggestions to the contrary (Lange and Carmichael, 1989; Ottonello et al., 2001) were not, therefore, substantiated. Thus it seems reasonable to rely on 298 K Mössbauer spectra for determination of Fe^{3+}/Fe^{2+} of the glasses.

The $Fe^{3+}/\Sigma Fe$ from the Mössbauer spectra (Table 3) is expressed as log Fe^{3+}/Fe^{2+} versus log f_{O_2} in Fig. 7. Such plots normally are straight lines with a slope near 0.25 when the melt composition does not vary with f_{O_2} (Mysen and Virgo, 1989; Mysen et al., 1984, 1985a; Jayasuriya et al., 2004). In Fig. 7, this relationship has some curvature in particular for the FD composition. This curvature is because the composition of melts coexisting with olivine (and spinel) depends on the oxygen fugacity (Table 2). Nonlinear relations such as shown in Fig. 7 therefore would be expected.

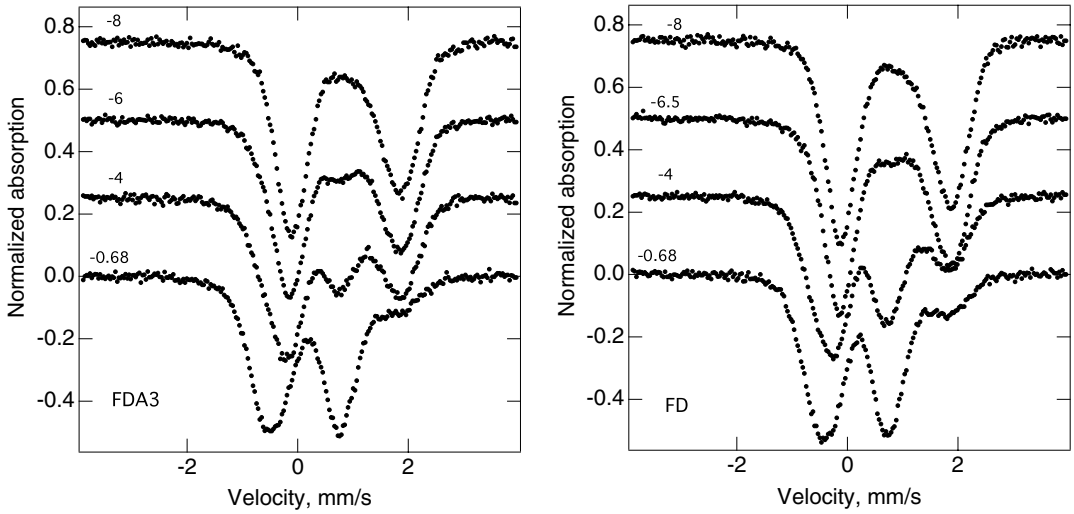

Fig. 5. Comparison of ^{57}Fe resonant absorption Mössbauer spectra (normalized to total absorption envelope) as a function of log f_{O_2} (indicated on individual spectra) of quenched melts in equilibrium with olivine at 1300 °C (FDA3) and 1375 °C (FD).

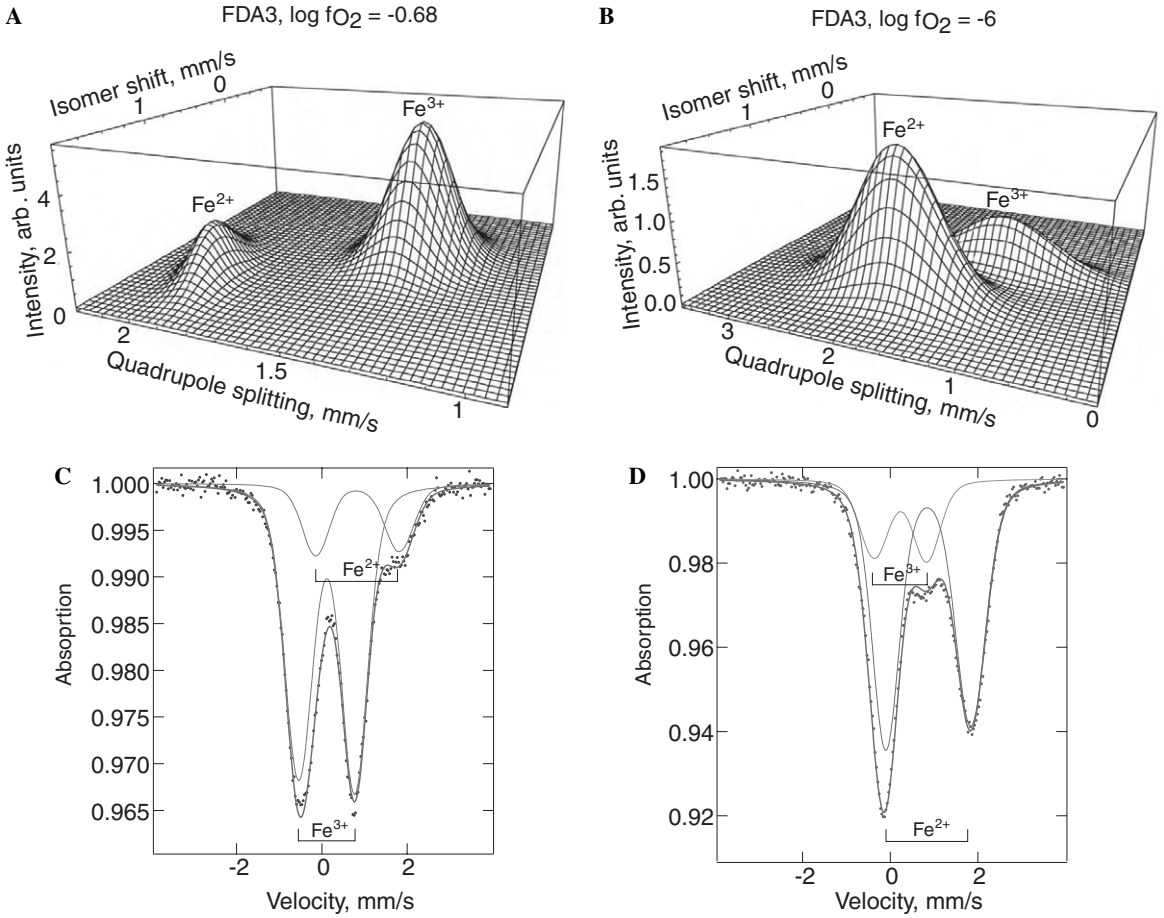

Fig. 6. Examples of fitted Mössbauer spectra of oxidized and reduced quenched FDA3 melts (glass). (A) Total probability function oxidized glass. (B) Total probability function of reduced glass. (C) Fitted absorption doublet of oxidized glass. (D) Fitted absorption doublet of reduced glass.

Hyperfine parameters, isomer shift and quadrupole splitting, are sensitive to local structure around the Fe nuclei. The full width at half height of the Δ-probability functions, $w_{\Delta Fe^{3+}}$ and $w_{\Delta Fe^{2+}}$ (Table 3), reflects a range of distortion of the Fe^{3+}–O and Fe^{2+}–O polyhedra, whereas the $w_{\delta Fe^{3+}}$- and $w_{\delta Fe^{2+}}$-values (Table 3) manifest ranges of Fe^{3+}–O and Fe^{2+}–O bond distance (Rancourt, 1994; Johnson et al., 1999). For Fe^{3+}, the isomer shift and quadrupole split distributions are distinctly narrower with $Fe^{3+}/\Sigma Fe$ less than about 0.4. Thus, the range in Fe–O distance and polyhedral distortion appears dependent on the $Fe^{3+}/\Sigma Fe$ and possibly also on bulk melt composition.

For iron-bearing crystalline materials, there are systematic relations between the isomer shift of Fe^{3+} and the oxygen coordination number (Burns, 1994). The $\delta_{Fe^{3+}}$ is less than about 0.35 mm/s (at 298 K) for 4-fold coordination, whereas $\delta_{Fe^{3+}}$-values above about 0.4 mm/s are typical for Fe^{3+} in 6-fold coordination with oxygen. This empirical relationship is consistent with larger Fe^{3+}–O bond distance the larger the coordination number. One might suggest, therefore, that the $\delta_{Fe^{3+}}$ trends in Fig. 8 imply a gradual transformation of Fe^{3+} to higher coordination as a function of decreasing $Fe^{3+}/\Sigma Fe$. This agrees with earlier suggestions that the structural role of ferric iron in silicate glasses and melts depends on the ferric/ferrous ratio (O'Horo and Levy, 1978; Virgo and Mysen, 1985; Dingwell and Virgo, 1987; Kress and Carmichael, 1991). The width of the probability functions (Table 3) implies, however, that there is a range in Fe^{3+}–O distances. Such a range might suggest that there could be a range in oxygen coordination numbers around ferric iron (e.g., Jackson et al., 2005). The average coordination number is, however, that inferred from the average $\delta_{Fe^{3+}}$. When discussing the relationship between redox ratio of iron and melt structure, we will use the average coordination number.

3.3. Olivine/melt partitioning and redox relations of iron

The relationships in Fig. 7 were used to derive redox ratio of iron for the samples for which Mössbauer data were not recorded. The relationship between $D_{Fe^{2+}}{}^{ol\text{-}melt}$ and oxygen fugacity was then obtained (Fig. 9). The $D_{Fe^{2+}}{}^{ol\text{-}melt}$-values differ substantially from the $D_{\Sigma Fe}{}^{ol\text{-}melt}$-values in Fig. 4 because the ferric iron content of the melts is subtracted. There remains, though, variation of $D_{Fe^{2+}}{}^{ol\text{-}melt}$ as a function of oxygen fugacity. This behavior resembles that of the other partition coefficients (Fig. 4).

Table 3
Mössbauer data

Ferric iron (Fe^{3+})											
Comp	log f_{O_2}	T (°C)	Fe^{3+}/Fe	$\delta_{Fe^{3+}}$ [a] (mm/s)	$s\delta_{Fe^{3+}}$ [b] (mm/s)	$\Delta_{Fe^{3+}}$ (mm/s)	$s\Delta_{Fe^{3+}}$ (mm/s)	$\sigma\delta_{Fe^{3+}}$ (mm/s)	$s\sigma\delta_{Fe^{3+}}$ (mm/s)	$\Delta\delta_{Fe^{3+}}$ (mm/s)	$s\Delta\delta_{Fe^{3+}}$ (mm/s)
FDA3	−0.68	1300	0.805	0.289	0.002	1.322	0.003	0.255	0.003	0.097	0.015
FDA3	−4	1300	0.447	0.330	0.006	1.230	0.006	0.273	0.006	0.06	0.023
FDA3	−6	1300	0.232	0.410	0.01	1.200	0.017	0.121	0.078	0.459	0.062
FDA3	−8	1300	0.118	0.490	0.03	1.191	0.049	0.105	0.07	0.432	0.075
FD	−0.68	1375	0.792	0.299	0.004	1.254	0.004	0.240	0.005	0.097	0.026
FD	−4	1375	0.587	0.335	0.002	1.212	0.004	0.231	0.007	0.137	0.037
FD	−6.5	1375	0.172	0.469	0.016	1.137	0.023	0.177	0.046	0.444	0.082
FD	−8	1375	0.092	0.480	0.031	1.225	0.048	0.161	0.074	0.339	0.015
Ferrous iron (Fe^{2+})											
Comp	logf_{O_2}	T (°C)	Fe^{2+}/Fe	$\delta_{Fe^{2+}}$ (mm/s)	$s\delta_{Fe^{2+}}$ (mm/s)	$\Delta_{Fe^{2+}}$ (mm/s)	$s\Delta_{Fe^{2+}}$ (mm/s)	$\sigma\delta_{Fe^{2+}}$ (mm/s)	$s\sigma\delta_{Fe^{2+}}$ (mm/s)	$\Delta\delta_{Fe^{2+}}$ (mm/s)	$s\Delta\delta_{Fe^{2+}}$ (mm/s)
FDA3	−0.68	1300	0.805	1.016	0.006	1.959	0.012	0.271	0.008	0.060	0.040
FDA3	−4	1300	0.447	1.047	0.003	1.949	0.005	0.256	0.003	0.044	0.021
FDA3	−6	1300	0.232	1.045	0.002	1.938	0.005	0.176	0.039	0.405	0.066
FDA3	−8	1300	0.118	1.058	0.003	1.938	0.008	0.197	0.012	0.332	0.026
FD	−0.68	1375	0.792	1.027	0.005	1.981	0.011	0.254	0.013	0.329	0.020
FD	−4	1375	0.587	1.041	0.003	1.926	0.008	0.225	0.008	0.284	0.030
FD	−6.5	1375	0.172	1.047	0.002	1.976	0.006	0.168	0.016	0.352	0.029
FD	−8	1375	0.092	1.051	0.002	1.961	0.006	0.179	0.012	0.326	0.024

δ, isomer shift; Δ, quadrupole splitting; and σ, FWHH of probability function.
[a] Isomer shift, δ, relative of Fe metal.
[b] Uncertainty (±1s fitting error).

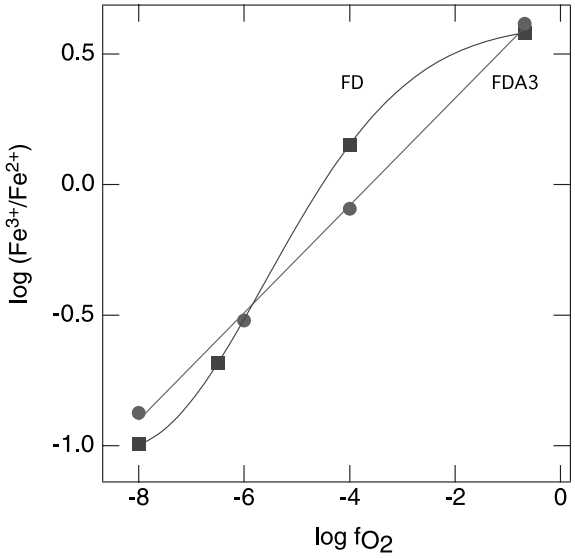

Fig. 7. Log (Fe^{3+}/Fe^{2+}) versus log f_{O_2} of glasses from FDA3 and FD composition. The FDA3-data were fitted to a straight line, whereas the FD data were fitted to a Gaussian function. These fits were chosen simply to satisfy the data. See also text for further discussion.

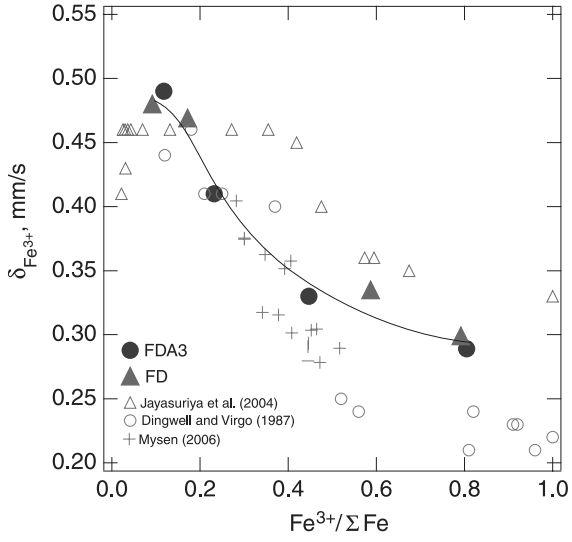

Fig. 8. Isomer shift of Fe^{3+}, $\delta_{Fe^{3+}}$ (mm/s relative to Fe metal) as a function of $Fe^{3+}/\Sigma Fe$. Also shown are data from Dingwell and Virgo (1987) from glasses in the system Na_2O–FeO–Fe_2O_3–SiO_2, from Jayasuriya et al. (2004) from glasses on the 0.1 MPa eutectic on the join $CaMgSi_2O_6$–$CaAlSi_2O_8$, and from Mysen (2006) for glasses in the system Na_2O–CaO–MgO–FeO–Fe_2O_3–Al_2O_3–SiO_2.

It is sometimes suggested that the exchange equilibrium constants, $K_{i-Mg}{}^{ol\text{-}melt}$, for an equilibrium of the type

$$Mg^{melt} + i^{olivine} = i^{melt} + Mg^{olivine} \quad (2)$$

may not be significantly dependent on melt composition. In fact, it has been suggested that melt structure effects on partition coefficients might be embodied in the MgO content of the melt (Hart and Davis, 1978).

The exchange coefficients, $K_{Fe^{2+}-Mg}{}^{ol\text{-}melt}$, $K_{Ca-Mg}{}^{ol\text{-}melt}$, $K_{Mn-Mg}{}^{ol\text{-}melt}$, $K_{Co-Mg}{}^{ol\text{-}melt}$, and $K_{Ni-Mg}{}^{ol\text{-}melt}$, are, however, dependent of oxygen fugacity, with those of the transition metals, Fe^{2+}, Ni^{2+}, and Co^{2+} showing a distinct minimum at intermediate f_{O_2}-values, and those of Mn and Ca increasing monotonously with decreasing f_{O_2} (Figs. 10

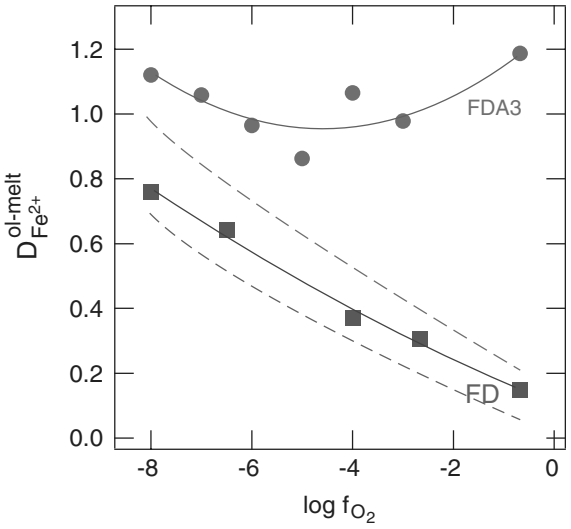

Fig. 9. Olivine/melt partition coefficient, $D_{Fe^{2+}}^{ol\text{-}melt}$, as a function of f_{O_2} for compositions FDA3 and FD. Also shown in dashed lines is $D_{\Sigma Fe}^{ol\text{-}melt}$ as a function of f_{O_2} from Fig. 4.

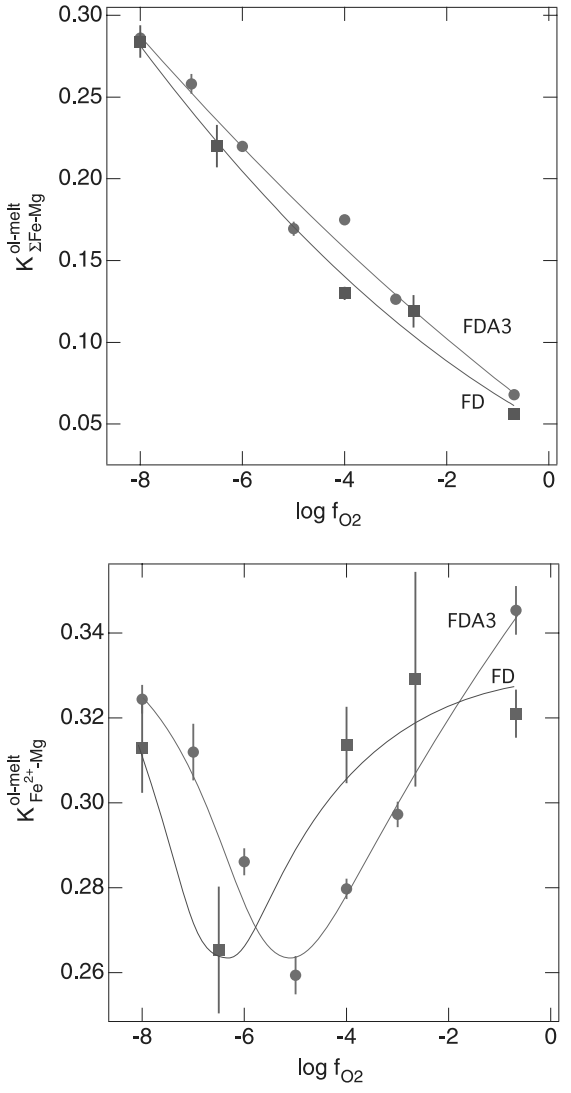

Fig. 10. Olivine/melt exchange coefficients, $K_{\Sigma Fe\text{–}Mg}^{ol\text{-}melt}$ and $K_{Fe^{2+}\text{–}Mg}^{ol\text{-}melt}$ as a function of f_{O_2}.

and 11). The difference between $K_{\Sigma Fe\text{–}Mg}^{ol\text{-}melt}$ and $K_{Fe^{2+}\text{–}Mg}^{ol\text{-}melt}$ is also evident (Fig. 10). There is a strong f_{O_2} effect on the $K_{\Sigma Fe\text{–}Mg}^{ol\text{-}melt}$ because of the ferric iron content of the melt decreases with decreasing f_{O_2}. The $K_{Fe^{2+}\text{–}Mg}^{ol\text{-}melt}$ also depends on f_{O_2}, however. Its behavior with f_{O_2}, which has a minimum at intermediate f_{O_2}-values, resembles that of $K_{Co\text{–}Mg}^{ol\text{-}melt}$ and $K_{Ni\text{–}Mg}^{ol\text{-}melt}$ (Fig. 11). There appear, therefore, to be changes in melt structure, induced by the change of redox ratio of iron. These changes may affect both the partition coefficients (Figs. 4 and 9) and the exchange equilibrium coefficients (Figs. 10 and 11).

4. Discussion

Mineral/melt element partition coefficients depend on melt structure (e.g., Mysen and Virgo, 1980; Kohn and Schofield, 1994; Jaeger and Drake, 2000; Toplis and Corgne, 2002; Mysen and Dubinsky, 2004). Melt structure is affected by the redox ratio of iron. Partition coefficients must also, therefore, depend on the redox ratio of iron.

How the redox relations affect melt structure depends on the roles of Fe^{3+} and Fe^{2+} in the melts. With Fe^{3+} as a network-former and Fe^{2+} as a network-modifier, one may write the redox reaction (Holmquist, 1966):

$$4FeO_2^- = 4Fe^{2+} + O_2 + 6O^{2-} \quad (3)$$

In Eq. (3), the oxygen anion, O^{2-}, is the link to the silicate network via a schematic depolymerization such as

$$2Q^4 + O^{2-} = 2Q^3, \quad (4)$$

where Q^4 is a fully polymerized structural unit (NBO/Si = 0) and Q^3 is a depolymerized unit (NBO/Si = 1). Equations similar to (4) can, of course, be written for other Q^n-species pairs, but the principle is the same. Reduction of network-forming Fe^{3+} to network-modifying Fe^{2+} results, therefore, in depolymerization of the silicate network:

$$4FeO_2^- + 12Q^4 = 12Q^3 + 4Fe^{2+} + O_2 \quad (5)$$

With both ferric and ferrous iron as network-modifiers, we can write a simple redox reaction of the type:

$$2Fe^{3+} + 2O^{2-} = 2Fe^{2+} + O_2 \quad (6)$$

which combined with Eq. (4) yields:

$$2Fe^{3+} + 2Q^3 = 2Fe^{2+} + 2Q^4 + O_2. \quad (7)$$

In this case, reduction of Fe^{3+} to Fe^{2+} causes silicate melt polymerization.

The isomer shift data in Fig. 8 indicate that the coordination number of Fe^{3+} is correlated with $Fe^{3+}/\Sigma Fe$. Reduction of Fe^{3+} with $Fe^{3+}/\Sigma Fe > 0.4$ causes silicate depolymerization perhaps according to Eq. (5), whereas for melts with $Fe^{3+}/\Sigma Fe < 0.4$, ferric iron undergoes coordination transformation and an expression such as (7), which is a polymerization reaction, may describe the relationship between Fe^{3+}/Fe^{2+} and melt polymerization. This reaction becomes increasingly important as $Fe^{3+}/\Sigma Fe$ decreases from ~0.4 to smaller values. Redox effects on sil-

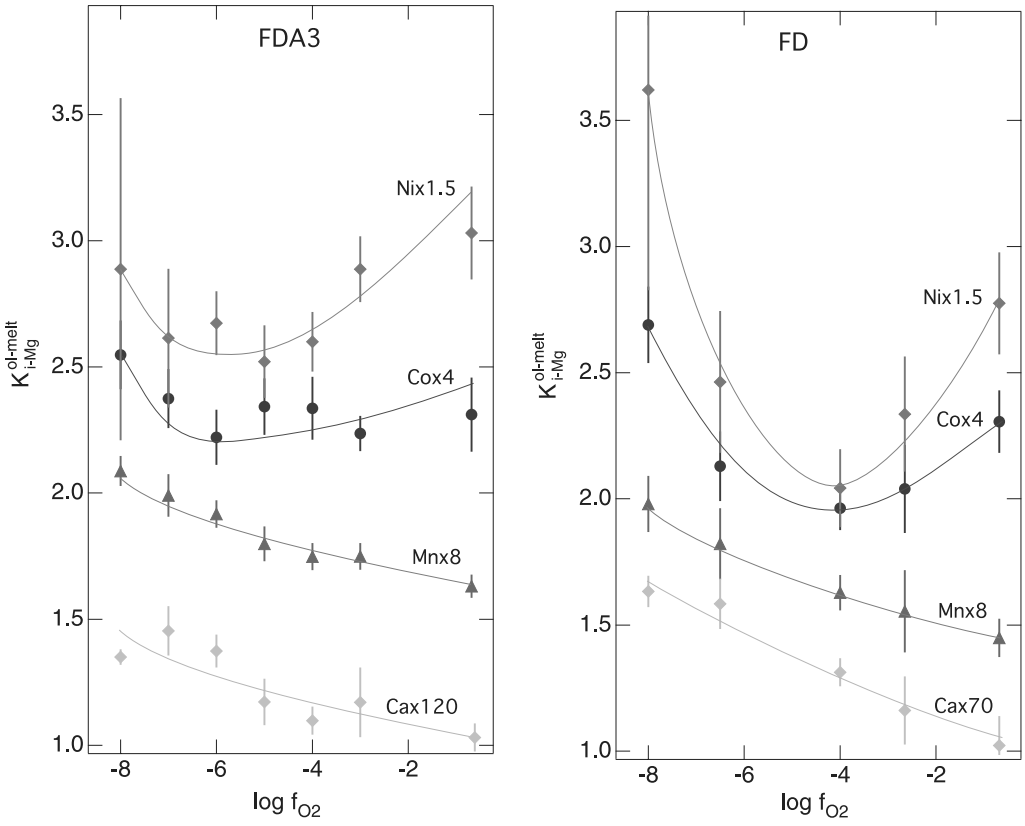

Fig. 11. Olivine/melt exchange coefficients, $K_{Ni\text{–}Mg}{}^{ol\text{-}melt}$, $K_{Co\text{–}Mg}{}^{ol\text{-}melt}$, $K_{Mn\text{–}Mg}{}^{ol\text{-}melt}$, $K_{Ca\text{–}Mg}{}^{ol\text{-}melt}$, as a function of f_{O_2}. Note the multipliers used for ease of display.

icate melt structure have been observed in the behavior of an NBO/T-sensitive property such as high-temperature melt viscosity (Dingwell and Virgo, 1987, 1988; Dingwell, 1991). Polymerization effects can also be seen in liquidus phase relations of iron-bearing silicate melts (Mysen et al., 1984).

In order to quantify the relationships between $Fe^{3+}/\Sigma Fe$ and melt polymerization, NBO/T, it was assumed that Fe^{3+} in the three most reduced samples is a network-modifier. Their $\delta_{Fe^{3+}}$ at 298 K is nearly constant near 0.45 mm/s (Fig. 8). Ferric iron in the two most oxidized samples is assumed to exist only as network-former as their $\delta_{Fe^{3+}}$ is near 0.3 mm/s (Fig. 8) For $Fe^{3+}/\Sigma Fe$-values intermediate between these extremes, there is an intermediate $\delta_{Fe^{3+}}$-value reflecting a fraction, x, of Fe^{3+} in tetrahedral coordination, $Fe^{3+}(IV)$, and a fraction, $(1-x)$, of Fe^{3+} in octahedral coordination, $Fe^{3+}(IV)$ so that

$$x\delta_{Fe^{3+}}(IV) + (1-x)\delta_{Fe^{3+}}(VI) = \delta_{Fe^{3+}}. \quad (8)$$

The NBO/T of the melts coexisting with olivine as a function of f_{O_2} from such calculations are shown in Fig. 12. For comparison, the dashed lines are the NBO/T-values calculated under the assumption that all iron, whether Fe^{3+} or Fe^{2+}, was network modifying. Thus, reduction of Fe^{3+} to Fe^{2+} results in about 100% increase in NBO/T of melts from FDA3 and between 250% and 300% for melts from composition FD (Fig. 12). The slight turnover of the curves at the lowest f_{O_2} reflects reduction of

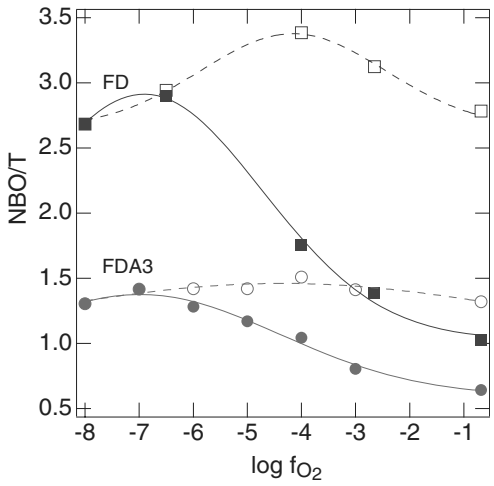

Fig. 12. Degree of polymerization, NBO/T, for melts coexisting with olivine as a function of f_{O_2}. Curves were fitted to Gaussian functions. Dashed lines represent the NBO/T trends calculated with all iron as network-modifying Fe^{2+}.

network-modifying Fe^{3+} to network-modifying Fe^{2+} dominating the equilibria. This latter reduction causes network polymerization.

There are distinct variations in $D_i^{ol\text{-}melt}$ ($i = Fe^{2+}$, Mg^{2+}, Mn^{2+}, Co^{2-}, Ni^{2+-}, Ca^{2+}) as a function of NBO/T of the melts calculated from the Mössbauer data (Fig. 13). For the Al-bearing FDA3 system, the partition coefficients pass

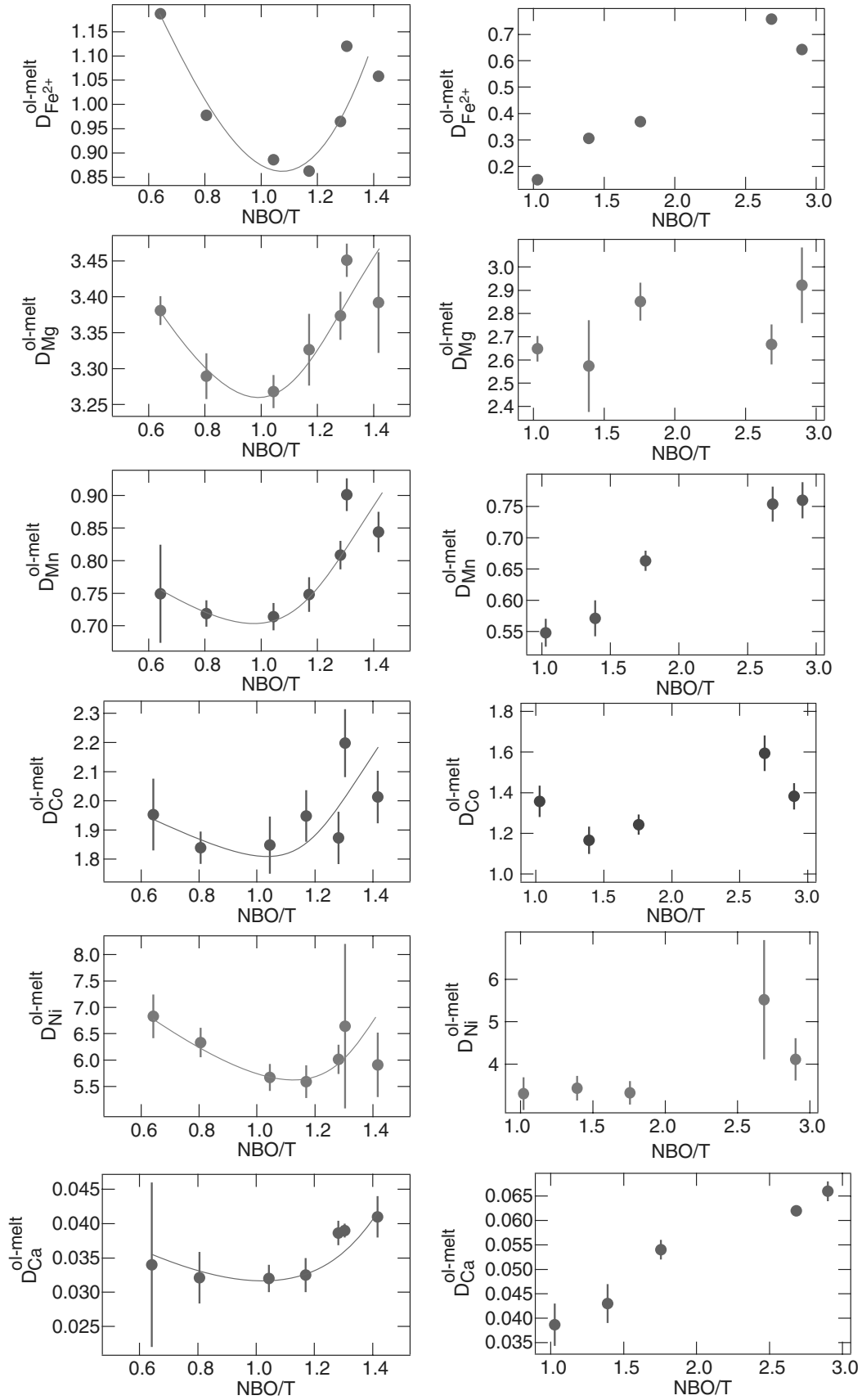

Fig. 13. Olivine/melt partition coefficients, $D_{Fe^{2+}}^{ol\text{-}melt}$, $D_{Mn}^{ol\text{-}melt}$, $D_{Mg}^{ol\text{-}melt}$, $D_{Ca}^{ol\text{-}melt}$, $D_{Co}^{ol\text{-}melt}$, and $D_{Ni}^{ol\text{-}melt}$ as a function of NBO/T of the melt calculated as discussed in the text. Left panels are for composition FDA3, whereas right panels are for FD.

through a minimum at NBO/T near 1. This NBO/T-value corresponds to $Fe^{3+}/\Sigma Fe$ between 0.34 and 0.44 (Table 2). For the FD system, the NBO/T of which increases from about 1 to about 3 with decreasing f_{O_2} (and $Fe^{3+}/\Sigma Fe$), the $D_i^{ol\text{-}melt}$ shows a slight (Mg^{2+}, Co^{2+}, Ni^{2+}) to distinct (Fe^{2+}, Mn^{2+}, Ca^{2+}) increase with increasing NBO/T (Fig. 13). There are no minima or maxima in the latter NBO/T-range, but this may be because the minimum observed in the FDA3 data occurs at an NBO/T-value near the minimum NBO/T-value of the FD data (NBO/T $\sim$ 1). It cannot be ruled out, however, the changes in charge-balance of tetrahedrally coordinated Al^{3+} in melts from the FDA3 system could also be the cause of the minimum. There is no Al^{3+}in the FD system.

The relationships between $K_{i\text{-}Mg}{}^{ol\text{-}melt}$ and NBO/T of the melt (Fig. 14) lead to the suggestion that with the premise discussed above that the activity coefficients of element, i, in olivine, $\gamma_i^{olivine}$, does not vary with olivine composition, the activity coefficients of element, i, in melt, γ_i^{melt}, does. We may, therefore, use the partitioning data to discuss variations in the activity coefficient ratio, $(\gamma_i/\gamma_{Mg})^{melt}$. This ratio is related to the exchange equilibrium coefficient, $K_{i\text{-}Mg}{}^{ol\text{-}melt}$, for Eq. (2) as

$$(\gamma_i/\gamma_{Mg})^{melt} = [K_{i\text{-}Mg}{}^{ol\text{-}melt}/K_{a(i\text{-}Mg)}{}^{ol\text{-}melt}][(\gamma_i/\gamma_{Mg})^{olivine}] \quad (9)$$

where $(\gamma_i/\gamma_{Mg})^{olivine}$ is constant. The $K_{a(i\text{-}Mg)}{}^{ol\text{-}melt}$ is the equilibrium constant for equilibrium (2) using activities rather than mol fractions. The $K_{a(i\text{-}Mg)}{}^{ol\text{-}melt}$ is also constant at constant temperature. Therefore, the activity coefficient ratio

$$(\gamma_i/\gamma_{Mg})^{melt} = \text{constant } K_{i\text{-}Mg}{}^{ol\text{-}melt}. \quad (10)$$

In other words, $(\gamma_i/\gamma_{Mg})^{melt}$, is proportional to the exchange equilibrium coefficient, $K_{i\text{-}Mg}{}^{ol\text{-}melt}$.

The $K_{i\text{-}Mg}{}^{ol\text{-}melt}$ is shown as function of melt NBO/T in Fig. 14. For composition FDA3, The $K_{Fe^{2+}\text{–}Mg}{}^{ol\text{-}melt}$, $K_{Ni\text{–}Mg}{}^{ol\text{-}melt}$ and, possibly $K_{Ni\text{–}Mg}{}^{ol\text{-}melt}$, and, therefore, their activity coefficient ratios, $(\gamma_i/\gamma_{Mg})^{melt}$, pass through a minimum at NBO/T between 1 and 1.2. For the other element pairs, whether in the FDA3 or FD systems, the activity coefficient ratio increases as a nonlinear function of NBO/T. All the activity coefficient ratios increase with NBO/T in the higher NBO/T-range ($\sim$1 to $\sim$3) of the FD-system (Fig. 14).

At least four melt structural factors may influence the changes in $(\gamma_i/\gamma_{Mg})^{melt}$. (i) Silicate melts (and glasses) can be described in terms of a distribution of Q^n units (number of bridging oxygens, $n = 0, 1, 2, 3, 4$). Their abundance depends on overall melt polymerization, NBO/T, and the ionization potential of network-modifying cations (Brawer

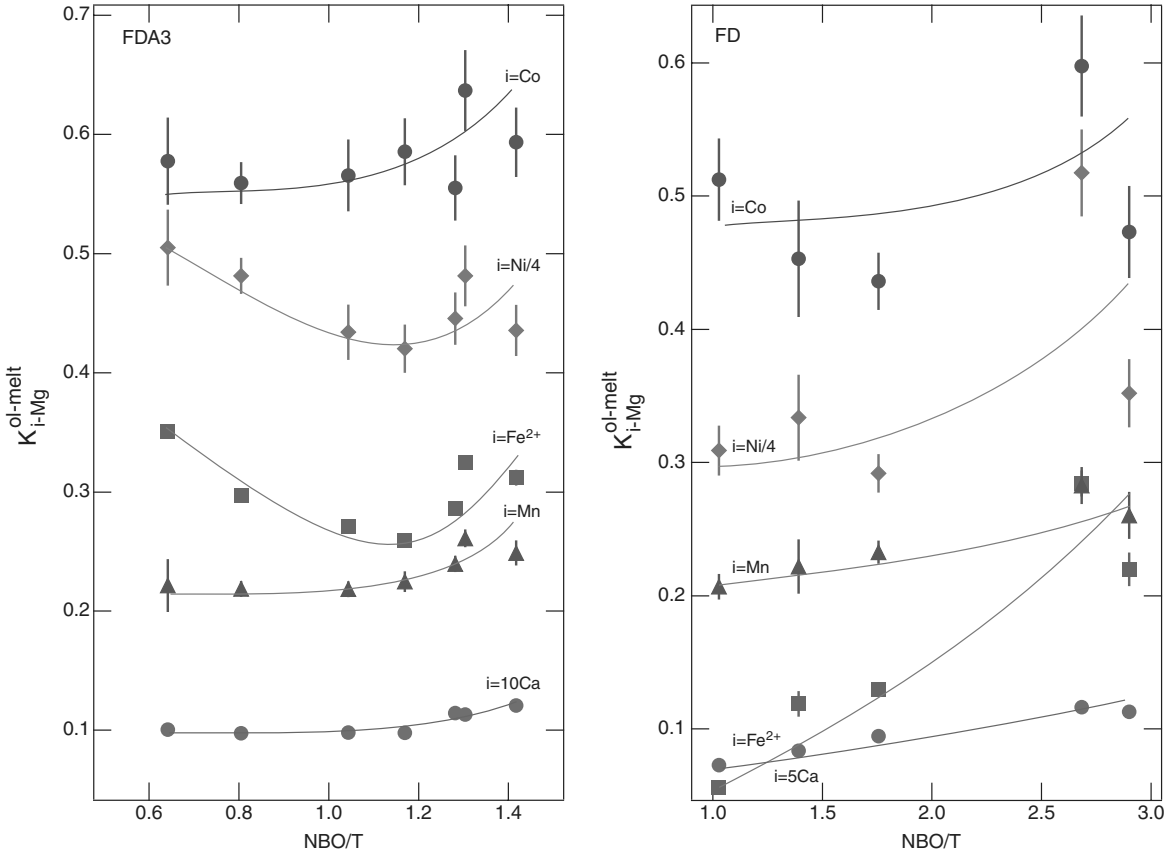

Fig. 14. Olivine/melt exchange coefficients, $K_{Fe^{2+}\text{–}Mg}{}^{ol\text{-}melt}$, $K_{Ni\text{–}Mg}{}^{ol\text{-}melt}$, $K_{Co\text{–}Mg}{}^{ol\text{-}melt}$, $K_{Mn\text{–}Mg}{}^{ol\text{-}melt}$, $K_{Ca\text{–}Mg}{}^{ol\text{-}melt}$, as a function of NBO/T of the melt calculated as discussed in the text. Note the multipliers used for ease of display.

and White, 1975, 1977; Virgo et al., 1980; Stebbins, 1987; Maekawa et al., 1991; Mysen, 1997, 2003). The nonbridging oxygens in these structural units are not energetically equivalent because the Si–NBO bond strength depends on the number of bridging oxygens in the structural unit. These differences are reflected, for example, in the frequencies in Raman and ^{29}Si NMR spectra of different Q^n species in melts (e.g., Furukawa et al., 1981; Engelhardt and Michel, 1987). This energetic nonequivalence results in ordering of network-modifying cations among different coexisting structural units (Jones et al., 2001; Lee and Stebbins, 2003) because steric hindrance leads to the cation with the smallest ionic radius or the largest electrical charge forming bonds with oxygen in the most depolymerized of available Q^n-units (Mysen and Dubinsky, 2004). The extent of ordering depends on types and abundance of nonbridging oxygen available in the coexisting Q^n-species. This, in turn, affects activity–composition relations in silicate melts. (ii) The coordination number of the cations in the melts may depend on melt polymerization. For example, the coordination number of Fe^{2+} appears dependent on melt polymerization and cation environment (see, for example, Rossano et al., 1999; Burkhard, 2000; Jackson et al., 2005) as does Ni^{2+} and possibly Co^{2+} (see, for example, Keppler, 1992; Keppler and Bagdassarov, 1999; Jackson et al., 2005). It is generally considered that Mn^{2+}, Ca^{2+} occupy structural positions with six or more oxygens in the coordination sphere (Keppler, 1992; Binsted et al., 1985). In addition, steric hindrance may cause distortion of the polyhedra. The extent of hindrance likely is a function of the types of nonbridging oxygen in the melt and becomes less severe the less polymerized the Q^n units in the melt (Mysen and Dubinsky, 2004). All these features can also affect activity–composition relations as a function of Q^n-type and abundance, which, in turn, may cause the nonlinear relationships between partition coefficients and NBO/T. (iii) Some of the cations may also serve to charge-balance tetrahedrally coordinated Al^{3+} in the FDA3 system. The relative stability of aluminate complexes in melts are systematic functions of the ionization potential of the charge-balancing cation (e.g., Navrotsky et al., 1985). When the $Fe^{3+}/\Sigma Fe$ changes, the charge-balance of Al^{3+} may also be affected, which could result in a change in $(\gamma_i/\gamma_{Mg})^{melt}$. (iv) Finally, there is spectroscopic and thermochemical evidence for stabilization of ferrite complexes by, for example, Fe^{2+},Fe^{3+} association (Virgo and Mysen, 1985; Kress and Carmichael, 1988). Whether other divalent transition metals may form analogous complexes is not known, but possible. The proportion and stability of such complexes likely will depend on the redox ratio of iron.

In summary, the relationships between olivine/melt partition coefficients and oxygen fugacity of Fe-bearing systems reflect changes in $Fe^{3+}/\Sigma Fe$ of the melts controlled by f_{O_2}. These changes, in turn, result in variations in melt polymerization, Q^n-speciation, cation distribution among the nonbridging oxygen in the Q^n-species, and changes in charge-balance of cations in 4-fold coordination (Fe^{3+} and Al^{3+}). These factors together govern the activity–composition relations in melts and, therefore, the effects of f_{O_2} on olivine/melt partitioning in Fe-bearing systems.

Acknowledgments

Critical reviews by Guy Libourel, Peter Ulmer, and the AE, Rick Ryerson, are appreciated. This research was conducted with partial support from NSF Grant EAR-0405383.

Associate editor: F.J. Ryerson

References

Alberto, H.V., Pinto da Cunha, J.L., Mysen, B.O., Gil, J.M., de Campos, N.A., 1996. Analysis of Mössbauer spectra of silicate glasses using a two-dimensional Gaussian distribution of hyperfine parameters. *J. Non-Cryst. Solids* **194**, 48–57.

Binsted, N., Greaves, G.N., Henderson, C.M.B., 1985. An EXAFS study of glassy and crystalline phases of compositions $CaAl_2Si_2O_8$ (anorthite) and $CaMgSi_2O_6$ (diopside). *Contrib. Mineral. Petrol.* **89**, 103–109.

Boström, D., 1987. Singe-crystal X-ray diffraction studies of synthetic Ni–Mg olivine solid solutions. *Am. Mineral* **72**, 965–972.

Brawer, S.A., White, W.B., 1975. Raman spectroscopic investigation of the structure of silicate glasses. I. The binary silicate glasses. *J. Chem. Phys.* **63**, 2421–2432.

Brawer, S.A., White, W.B., 1977. Raman spectroscopic investigation of the structure of silicate glasses. II. The soda-alkaline earth-alumina ternary and quarternary glasses. *J. Non-Cryst. Solids* **23**, 261–278.

Burkhard, D.J.M., 2000. Iron-bearing silicate glasses at ambient conditions. *J. Non-Cryst. Solids* **275**, 175–188.

Burns, R.G., 1994. Mineral Mössbauer spectroscopy: correlations between chemical shift and quadrupole splitting parameters. *Hyperfine Interact.* **91**, 739–745.

Calas, G., Petiau, J., 1983. Coordination state of iron in oxide glasses through high-resolution K-edge spectra: information from pre-edge. *Solid State Commun.* **48**, 625–629.

Dingwell, D.B., 1991. Redox viscometry of some Fe-bearing silicate melts. *Am. Mineral.* **76**, 1560–1562.

Dingwell, D.B., Virgo, D., 1987. The effect of oxidation state on the viscosity of melts in the system Na_2O–FeO–Fe_2O_3–SiO_2. *Geochim. Cosmochim. Acta* **51**, 195–205.

Dingwell, D.B., Virgo, D., 1988. Viscosities of melts in the Na_2O–FeO–Fe_2O_3–SiO_2 systems and factors-controlling relative viscosities in fully polymerized melts. *Geochim. Cosmochim. Acta* **52**, 395–404.

Doyle, C.D., Naldrett, A.J., 1987. Ideal mixing of divalent cations in mafic magma: II. The solution of NiO and the partitioning of nickel between coexisting olivine and liquid. *Geochim. Cosmochim. Acta* **51**, 213–219.

Dyar, M.D., Naney, M.T., Swanson, S.E., 1987. Effect of quench methods on Fe^{3+}/Fe^{2+} ratios: a Mössbauer and wet chemical study. *Am. Mineral.* **72**, 792–800.

Engelhardt, G., Michel, D., 1987. *High-Resolution Solid-State NMR of Silicates and Zeolites*. Wiley.

Furukawa, T., Fox, K.E., White, W.B., 1981. Raman spectroscopic investigation of the structure of silicate glasses. III. Raman intensities and structural units in sodium silicate glasses. *J. Chem. Phys.* **153**, 3226–3237.

Gaillard, F., Pichavant, M., Scaillet, B., 2003. Experimental determination of the activities of FeO and Fe_2O_3 components in hydrous silicic melts under oxidizing conditions. *Geochim. Cosmochim. Acta* **67**, 4389–4410.

Hart, S.R., Davis, K.E., 1978. Nickel partitioning between olivine and silicate melt. *Earth Planet. Sci. Lett.* **40**, 203–220.

Holland, D., Mekki, A., Gee, I.A., McConville, C.F., Johnson, J.A., Johnson, C.E., Appleyard, P., Thomas, M., 1999. The structure of sodium iron silicate glass—a multi-technique approach. *J. Non-Cryst. Solids* **253**, 192–202.

Holmquist, S., 1966. Ionic formulation of redox equilibria in glass melts. *J. Am. Ceram. Soc.* **49**, 228–229.

Holzheid, A., Palme, H., Chakraborty, S., 1997. The activities of NiO, CoO, and FeO in silicate melts. *Chem. Geol.* **139**, 21–38.

Jackson, W.E., Farges, F., Yeager, M., Mabrouk, P.A., Rossano, S., Waychunas, G.A., Solomon, E.I., Brown, G.E., 2005. Multispectroscopic study of Fe(II) in silicate glasses: implications for the coordination environment of Fe(II) in silicate melts. *Geochim. Cosmochim. Acta* **69**, 4315–4332.

Jaeger, W.L., Drake, M.J., 2000. Metal-silicate partitioning of Co, Ga, and W; dependence on silicate melt composition. *Geochim. Cosmochim. Acta* **64**, 3887–3895.

Jayasuriya, K., O'Neill, H.S.C., Berry, A.J., Campbell, S.J., 2004. A Mössbauer study of the oxidation state of Fe in silicate melts. *Am. Mineral.* **89**, 1597–1609.

Johnson, J.A., Johnson, C.E., Holland, D., Mekki, A., Appleyard, P., Thomas, M.F., 1999. Transition metal ions in ternary sodium silicate glasses: a Mössbauer and neutron study. *J. Non-Cryst. Solids* **246**, 104–114.

Jones, A.R., Winter, R., Greaves, G.N., Smith, I.H., 2001. MAS NMR study of soda-lime-silicate glasses with variable degrees of polymerisation. *J. Non-Cryst. Solids* **293–295**, 87–92.

Jurewicz, A.J.G., Watson, E.B., 1988. Cations in olivine. Part I: Calcium partitioning and calcium–magnesium distribution between olivines and coexisting melts, with petrological applications. *Contrib. Mineral. Petrol.* **99**, 176–185.

Keppler, H., 1992. Crystal field spectra and geochemistry of transition metal ions in silicate melts and glasses. *Am. Mineral.* **77**, 62–75.

Keppler, H., Bagdassarov, N.S., 1999. The speciation of Ni and Co in silicate melts from optical absorption spectra to 1500 °C. *Chem. Geol.* **158**, 105–115.

Kohn, S.C., Schofield, P.F., 1994. The importance of melt composition in controlling trace-element behaviour: an experimental study of Mn and Zn partitioning between forsterite and silicate melt. *Chem. Geol.* **117**, 73–87.

Kress, V.C., Carmichael, I.S.E., 1988. Stoichiometry of the iron oxidation reaction in silicate melts. *Am. Mineral.* **73**, 1267–1274.

Kress, V.C., Carmichael, I.S.E., 1991. The compressibility of silicate liquids containing Fe_2O_3 and the effect of composition, temperature, oxygen fugacity and pressure on their redox states. *Contrib. Mineral. Petrol.* **108**, 82–92.

Kushiro, I., 1975. On the nature of silicate melt and its significance in magma genesis: regularities in the shift of liquidus boundaries involving olivine pyroxene, and silica materials. *Am. J. Sci.* **275**, 411–431.

Lagarec, K., Rancourt, D.G., 1997. Extended Voigt-based analytical lineshape method for determining N-dimensional correlated hyperfine parameter distributions in Mössbauer spectroscopy. *Nucl. Instr. Methods Phys. Res. Sect. B* **129**, 266–280.

Lange, R.A., Carmichael, I.S.E., 1989. Ferric–ferrous equilibria in Na_2O–FeO–Fe_2O_3–SiO_2 melts: effects of analytical techniques on derived partial molar volumes. *Geochim. Cosmochim. Acta* **53**, 2195–2204.

Lee, S.K., Stebbins, J.F., 2003. Nature of cation mixing and ordering in Na–Ca silicate glasses and melts. *J. Phys. Chem. B* **107**, 3141–3148.

Libourel, G., 1999. Systematics of calcium partitioning between olivine and silicate melt: implications for melt structure and calcium content of magmatic olivines. *Contrib. Mineral. Petrol.* **136**, 63–80.

Maekawa, H., Maekawa, T., Kawamura, K., Yokokawa, T., 1991. The structural groups of alkali silicate glasses determined from ^{29}Si MAS–NMR. *J. Non-Cryst. Solids* **127**, 53–64.

Mysen, B.O., 1988. *Structure and Properties of Silicate Melts*. Elsevier, Amsterdam.

Mysen, B.O., 1997. Aluminosilicate melts: structure, composition and temperature. *Contrib. Mineral. Petrol* **127**, 104–118.

Mysen, B.O., 2003. Physics and chemistry of silicate glasses and melts. *Eur. J. Mineral* **15**, 781–802.

Mysen, B.O., 2006. The structural behavior of ferric and ferrous iron in aluminosilicate glass near meta-aluminosilicate joins. Geochim. Cosmochim. Acta, in press.

Mysen, B.O., Virgo, D., 1980. Trace element partitioning and melt structure: an experimental study at 1 atm pressure. *Geochim. Cosmochim. Acta* **44**, 1917–1930.

Mysen, B.O., Virgo, D., 1989. Redox equilibria, structure, and properties of Fe-bearing aluminosilicate melts: relationships between temperature, composition, and oxygen fugacity in the system Na_2O–Al_2O_3–SiO_2–Fe–O. *Am. Mineral.* **74**, 58–76.

Mysen, B.O., Dubinsky, E., 2004. Mineral/melt element partitioning and melt structure. *Geochim. Cosmochim. Acta* **68**, 1617–1634.

Mysen, B.O., Richet, P., 2005. *Silicate Glasses and Melts—Properties and Structure*. Elsevier, Amsterdam, p. 544.

Mysen, B.O., Seifert, F., Virgo, D., 1980. Structure and redox equilibria of iron-bearing silicate melts. *Am. Mineral.* **65**, 867–884.

Mysen, B.O., Virgo, D., Seifert, F.A., 1984. Redox equilibria of iron in alkaline earth silicate melts: relationships between melt structure, oxygen fugacity, temperature and properties of iron-bearing silicate liquids. *Am. Mineral.* **69**, 834–848.

Mysen, B.O., Virgo, D., Neumann, E.R., Seifert, F.A., 1985a. Redox equilibria and the structural states of ferric and ferrous iron in melts in the system CaO–MgO–Al_2O_3–SiO_2: relations between redox equilibria, melt structure and liquidus phase equilibria. *Am. Mineral.* **70**, 317–322.

Mysen, B.O., Carmichael, I.S.E., Virgo, D., 1985b. A comparison of iron redox ratios in silicate glasses determined by wet- chemical and ^{57}Fe Mössbauer resonant absorption methods. *Contrib. Mineral. Petrol.* **90**, 101–106.

Navrotsky, A., Geisinger, K.L., McMillan, P., Gibbs, G.V., 1985. The tetrahedral framework in glasses and melts—influences from molecular orbital calculations and implications for structure, thermodynamics, and physical properties. *Phys. Chem. Minerals* **11**, 284–298.

O'Horo, M.P., Levy, R.A., 1978. Effect of melt atmosphere on the magnetic properties of a $[(SiO_2)_{45}\ (CaO)_{55}]_{65}\ [Fe_2O_3]_{35}$ glass. *J. Appl. Phys.* **49**, 1635–1637.

O'Neill, H.S.C., Eggins, S.M., 2002. The effect of melt composition on trace element partitioning: an experimental investigations of the activity coefficients of FeO, NiO, CoO, MoO_2 and MoO_3 in silicate melts. *Chem. Geol.* **186**, 151–181.

Ottonello, G., Della Giusta, A., Molin, G.M., 1989. Cation ordering in Ni–Mg olivines. *Am. Mineral.* **74**, 411–412.

Ottonello, G., Moretti, R., Marini, L., Zuccholini, M.V., 2001. Oxidation state of iron in silicate glasses and melts: a thermochemical model. *Chem. Geol.* **174**, 157–179.

Presnall, D.C., Brenner, N.L., 1974. A method for studying iron silicate liquids under reducing conditions with negligible iron-loss. *Geochim. Cosmochim. Acta* **38**, 1785–1788.

Rancourt, D.A., 1994. Mössbauer spectroscopy of minerals 1. Inadequacy of Lorentzian-line doublets in fitting spectra arising from quadrupole splitting distributions. *Phys. Chem. Minerals* **21**, 244–249.

Rossano, S., Behrens, H., Morin, G., Bauer, J.-P., Brouder, C., Calas, G., 1999. Study of iron oxidation state of tektites by Mössbauer effect. *Phys. Chem. Minerals* **26**, 530–538.

Rossano, S., Ramos, A.Y., Delaye, J.M., 2000. Environment of ferrous iron in $CaFeSi_2O_6$ glass: contributions of EXAFS and molecular dynamics. *J. Non-Cryst. Solids* **273**, 48–52.

Ryerson, F.J., 1985. Oxide solution mechanisms in silicate melts: systematic variations in the activity coefficient of SiO_2. *Geochim. Cosmochim. Acta* **49**, 637–651.

Sato, M., 1972. Electrochemical measurements and control of oxygen fugacity and other gaseous fugacities with solid electrolyte system. In: Ulmer, G.C. (Ed.), *Research Techniques for High Pressure and High Temperature*. Springer Verlag, chapter 3.

Schwerdtfeger, K., Muan, A., 1966. Activities in olivine and pyroxenoid solid solutions of the system Fe–Mn–Si–O at 1150 °C. *Trans. Metal. Soc. AIME* **236**, 201–211.

Seifert, S., O'Neill, H.S.C., 1987. Experimental determination of activity–composition relations in Ni_2SiO_4–Mg_2SiO_4 and Co_2SiO_4–Mg_2SiO_4 olivine solid solutions at 1200 K and 0.1 MPa and 1573 L and 0.5 GPa. *Geochim. Cosmochim. Acta* **51**, 97–104.

Snyder, D.A., Carmichael, I.S.E., 1992. Olivine liquid equilibria and the chemical activities of FeO, NiO, Fe_2O_3, and MgO in natural basaltic melts. *Geochim. Cosmochim. Acta* **56**, 303–318.

Stebbins, J.F., 1987. Identification of multiple structural species in silicate glasses by ^{29}Si NMR. *Nature* **330**, 465–467.

Takahashi, E., 1978. Partitioning of Ni^{2+}, Co^{2+}, Fe^{2+}, Mn^{2+} and Mg^{2+} between olivine and silicate melts: compositional dependence of partition coefficients. *Geochim. Cosmochim. Acta* **42**, 1829–1845.

Toplis, M.J., 2004. The thermodynamics of iron and magnesium partitioning between olivine and liquid: Criteria for assessing and predicting equilibrium in natural and experimental systems. *Contr. Mineral. Petrol.* **149**, 22–39.

Toplis, J., Carroll, M.R., 1995. An experimental study of the influence of oxygen fugacity on Fe-Ti oxide stability, and mineral-melt equilibria in ferro-basaltic systems. *J. Petrol.* **36**, 1137–1170.

Toplis, M.J., Corgne, A., 2002. An experimental study of element partitioning between magnetite, clinopyroxene and iron-bearing silicate liquids with particular emphasis on vanadium. *Contrib. Mineral. Petrol* **144**, 22–37.

Tretyakov, J.D., Muan, A., 1969. A new cell for electrochemical studies at elevated temperatures: design and properties of a cell involving a combination of thorium oxide–yttrium oxide and zirconium oxide–calcium oxide electrolytes. *Am. Ceram. Soc.* **116**, 331–334.

Virgo, D., Mysen, B.O., 1985. The structural state of iron in oxidized vs. reduced glasses at 1 atm: a ^{57}Fe Mössbauer study. *Phys. Chem. Minerals* **12**, 65–76.

Virgo, D., Mysen, B.O., Kushiro, I., 1980. Anionic constitution of 1-atmosphere silicate melts: implications of the structure of igneous melts. *Science* **208**, 1371–1373.

Wang, Z., Cooney, T.F., Sharma, S.K., 1993. High temperature structural investigation of $Na_2O.0.5Fe_2O_3.3SiO_2$ and $Na_2O.FeO.3SiO_2$ melts and glasses. *Contrib. Mineral. Petrol.* **115**, 112–122.

Warner, R.D., Luth, W.C., 1974. The diopside-orthoenstatite two-phase region in the system $CaMgSi_2O_6$–$Mg_2Si_2O_6$. *Am. Mineral.* **59**, 98–109.

Watson, E.B., 1977. Partitioning of manganese between forsterite and silicate liquid. *Geochim. Cosmochim. Acta* **41**, 1363–1374.

Waychunas, G.A., Brown, G.E., Ponader, C.W., Jackson, W.E., 1988. Evidence from X-ray absorption for network-forming Fe^{2+} in molten alkali silicates. *Nature* **332**, 251–253.

Wilke, M., Behrens, H., Burkhard, D.J.M., Rossano, S., 2002. The oxidation state of iron in silicic melt at 500 MPa water pressure. *Earth Planet. Sci. Lett.* **189**, 55–67.